# X-ray Absorption Spectroscopy Studies of Thiolate-protected Gold Nanoclusters with FCC-, HCP- and BCC-like Core Geometry

By

Rui Yang

Submitted in partial fulfillment of the requirements
for the degree of Master of Science

at

Dalhousie University
Halifax, Nova Scotia
November 2017

# Table of Contents

# List of Tables

# List of Figures

# Abstract

Research on thiolate-protected gold nanoclusters (AuSR NCs) has recently attracted a great deal of interests due to their intriguing atomic structure and promising applications in catalysis, nanoelectronics, bio-detection, and so on. Among the AuSR NCs reported so far, the NCs with face centered cubic (FCC)-like core structure are particularly interesting because of its similar geometry to bulk gold. In addition, hexagonal-close-packed (HCP)-like and body-centered cubic (BCC)-like AuSR NCs have also been discovered recently, and thus it will be important to understand how such new core geometry will influence their bonding properties.

In this thesis, the focus is placed on the experimental and theoretical X-ray absorption spectroscopy (XAS) studies of the local structure and bonding properties of FCC-like, HCP-like and BCC-like AuSR NCs: $Au_{44}(SR)_{28}$, $Au_{30}(SR)_{18}$ and $Au_{38}S_2(SR)_{20}$. First, experimental XAS at Au $L_3$-edge was employed to investigate the bonding properties of $Au_{44}(SR)_{28}$. A multi-shell XAS fitting procedure was developed to probe its local structure from the gold perspective. In addition, temperature-dependent XAS was used to study the dynamic bonding behavior of the NCs. By comparing with the XAS fitting results of two other NCs, $Au_{28}(SR)_{20}$ and $Au_{36}(SR)_{24}$, a unique size-dependent trend was discovered for this series of FCC-like AuSR NCs. The size-dependent bonding behavior of these NCs was accounted for by closely examining the core structure of the three NCs. Second, Au $L_3$-edge XAS was used to study the bonding properties of HCP-like $Au_{30}(SR)_{18}$. By comparing with icosahedral-like $Au_{25}(SR)_{18}$ and FCC-like $Au_{36}(SR)_{24}$, X-ray absorption near edge structure (XANES) analysis in association with site-specific simulations was performed to study the bonding properties of surface gold sites. Temperature-dependent XAS measurements were employed to help to examine the thermal bonding behavior in the first Au-Au shells. Finally, the bonding properties of BCC-like $Au_{38}S_2(SR)_{20}$ was presented by comparing its XAS results with the bi-icosahedral like $Au_{38}(SR)_{24}$ due to their similar composition. XANES, together with site-specific simulations, was employed to study their bonding properties from the surface site perspective. The special surface Au-Au bonding properties of the BCC-like NCs were found to be connected with its unusual sulfide gold unit. The ligand effect on solvation-induced structure change was further investigated on these NCs by multi-shell EXAFS fitting, suggesting the ligand structure can be used to control the solution-phase bonding behavior of the NCs. Overall, this work highlights the important role of the core geometry in controlling the NC core, surface and ligand bonding behavior. The XAS methodology demonstrated in this thesis employing the first derivative XANES and simulations, in association with the multi-shell EXAFS analysis, can also be extended to the studies of other metal NC systems.

# List of Abbreviations and Symbols Used

| | |
|---|---|
| APS | Advanced Photon Source |
| BCC | Body centered cubic |
| CN | Coordination number |
| DFT | Density functional theory |
| DOS | Density of states |
| EXAFS | Extended X-ray absorption fine structure |
| FCC | Face-centered cubic |
| FT | Fourier-transformation |
| HCP | Hexagonal-close-packed |
| HOMO | Highest occupied molecular orbital |
| K | Kelvin |
| LOMO | Lowest unoccupied molecular orbital |
| LT | Low temperature |
| NC | Nanocluster |
| NP | Nanoparticle |
| NTE | Negative thermal expansion |
| R | Bond distance |
| RT | Room temperature |
| SPR | Surface plasmon resonance |

| | |
|---|---|
| SR | Thiolate ligands |
| XANES | X-ray absorption near-edge structure |
| XAS | X-ray absorption spectroscopy |
| $\sigma^2$ | Debye-Waller factor |
| $E_0$ | Absorption edge energy |
| $\Delta E_0$ | Energy shift |
| $\chi(k)$ | Modulation of the photoelectron wave |
| $\mu(E)$ | X-ray absorption coefficient |
| $f(k)$ | Scattering amplitude |
| $\delta(k)$ | Scattering phase shift |

# Acknowledgements

First, I would like to thank my supervisor, Dr. Peng Zhang, for his guidance and support in this work. Peng spent a lot of time to help me improve my scientific writing and learn how to solve scientific problems. I would also like to thank my supervisory committee member Dr. Heather Andreas for reading my thesis. I appreciate the help from all previous and current Zhan group members, especially Daniel Chevrier, Daniel Padmos, Paul Duchesne and Peter Cho. Furthermore, I would like to acknowledge all the beamline scientists (Yongfeng Hu, Ning Chen, Matthew Ward and Robert Gordon) and collaborators (Chenjie Zeng, Tatsuya Higaki and Dr. Rongchao Jin). Finally, I would like to thank my parents for their support and encouragement.

# Chapter 1 – Introduction

## 1.1 Overview of Noble Metal Nanoparticles

A general description of nanotechnology is the technological applications of engineered materials or devices with at least one dimension falling within the nanoscale (~1-100 nm).[1] Among the various materials being used in nanotechnology, noble metal nanoparticles (NPs) play a particularly important role.[2] Noble metal NPs can be prepared using a variety of approaches, such as the wet-chemical method.[3] This preparation method is useful in the control of NP size, shape and composition[4] which are fundamental for directing the NP properties.

The catalytic activity of noble metals is strongly dependent on their sizes and shapes.[5] In comparison with bulk metals, noble metal NPs have a higher surface-to-volume ratio. The larger surface area of NPs often leads to better catalytic performance.[6] As a result, size-controlled noble metal NPs are widely used in various catalysis processes.[7–9] For example, they can be used as electrocatalysts to catalyze fuel cell reactions.[10–12] Additionally, size can also have a dramatic effect on the electronic properties of noble metal NPs. For instance, when the size of metal particles is decreased to 1-2 nm, well-separated molecular orbitals will form, in contrast to the typical band structure for the bulk. As such, their catalytic properties will be significantly changed.[13]

The optical properties of NPs play an important role in their applications in biotechnology.[14] In 1908, Gustav Mie found the interaction between light and metal NPs can result in the resonant oscillations of conduction electrons on the NP surface. This phenomenon is known as surface plasmon resonance (SPR),[15] and the important formulation for handling particle-light interaction is generally referred to as Mie theory.[16] Based on the Mie theory, the SPR frequency depends on the composition, size and shape of NPs. For example, when the size of noble metals is reduced from bulk to nanoscale, their color in solution can often be changed.[2] That is because the NP size affects the oscillations of the surface electrons which will finally change the optical properties. Moreover, NPs can be prepared in various shapes, such as spheres,[17] wires,[18] tubes,[19] rods[20] and cubes.[21] The controlled shape can be used to tune the SPR features of the NPs, which is very useful in many SPR-related applications.[22,23] For example, silver nanorods have two SPR absorption peaks, while spherical silver NPs have only one SPR absorption peak. The extra SPR band will provide new opportunities for sensing applications.[24] In addition, SPR frequency is also related to the dielectric properties of the surrounding medium, and the inter-nanoparticle coupling interactions.[14] The sensitivity of the NP SPR frequency to the local medium dielectric constant can be used to generate a biosensor for the detection of an analyte.[25–27]

## 1.2 Gold Nanoparticles

Among all the metals, gold is the most stable and is one of the most frequently used elements in nanotechnology.[28] Gold nanoparticles (Au NPs), sometimes also called gold colloids or soluble gold, are known as the most stable metal NPs. The term "gold colloid" was named by Graham in 1861.[29] In fact, Au NPs have a much longer history than any other noble metal NPs. Around 4$^{th}$ or 5$^{th}$ century, "soluble" gold was found to be used in Egypt and China for medical purposes.[28] At the same time, people started to employ gold colloids to make ruby glass and to color ceramics.[30] However, the lack of stability of gold colloids limited further application.[28] As such, studies on how to make them more stable continued for a long time.[30] For example, in 1718, Hans Heinrich Helcher found the stability of soluble gold can be enhanced using boiled starch in the preparation process.[30]

It wasn't until the twentieth century that significant progress on Au NP synthesis was achieved. In 1951, Turkevitch reported the citrate reduction method to prepare Au NPs,[30] which has been widely used for several decades. In this method, citrate was used to both reduce $Au^{3+}$ and protect surface of Au NPs. However, the NPs prepared by this method are only stable in solution, thus limiting the application of the NPs. The most important finding on the preparation of stable Au NPs is perhaps the synthesis of thiolate-protected Au NPs in a two-phase liquid-liquid system published by Brust et al. in 1994.[31] The discovery of thiolate-protected Au NPs

successfully overcame the problem of low stability and allows the NPs to be dried and stored for a long time.

In the study of Au NPs, the optical and electronic properties are found to be largely dependent on the size, shape and surface chemistry.[4,28,32–34] In other words, the optical and electronic properties of Au NPs are tunable by controlling their structure. Au NPs can then be used in many applications based on these tunable properties. Au NPs with controllable optical properties are widely used for applications in nanotechnology such as bioimaging,[35,36] biosensors,[26,27] and optical coatings.[37] For example, Au NPs can be conjugated to specific antibodies and the modified surface can help them to enter malignant cells. By collecting SPR scattering images and SPR absorption spectra from these Au NPs, the anatomic labeling information can be achieved.[38] Secondly, Au NPs with tunable electronic properties show promising catalytic performances in a number of catalytic reactions such as CO oxidation[39] and acetylene hydrochlorination.[40] For instance, Au NPs supported on metal oxides such as $Co_3O_4$, $Fe_2O_3$, and $TiO_2$ can form an active interface along the perimeter of Au NPs, making them highly reactive in CO oxidation catalytic processes.[30]

## 1.3 Gold Nanoclusters

### 1.3.1 General background

Au NCs normally consist of 10s to 100s Au atoms and usually have a particle diameter less than 2 nm.[13,41] Unlike larger Au NPs, the ultra-small size of Au NCs induces distinctive quantum confinement effects, which result in discrete electronic structure and molecule-like properties, such as HOMO–LUMO electronic transition, enhanced photoluminescence, and intrinsic magnetism.[42–44] These unique properties make Au NCs promising for widespread applications such as catalysis[45,46] and bioimaging.[41,47]

To stabilize the Au NCs, various ligands are employed, such as the thiolate,[48] phosphine,[49] selenolate[50] and proteins.[41,51,52] One of the first Au NCs with precisely controlled structure was phosphine-protected $Au_{55}$ cluster reported by the Schmid's group in 1981.[53] Further analysis using EXAFS, reported by Cluskey et al., suggested the existence of both phosphine and chloride ligands on the surface of the NCs.[49]

Within the variety of useable protecting ligands, thiolate ligands show excellent stability and versatility in Au NC surface functionalization.[13,44] Unlike other ligands, thiolate on the surface of Au NCs can form very strong covalent bonds, helping to create a more stable NC structure.[13] Furthermore, the thiolate ligands are more widely available in various formats partially due to their natural existence in biomolecules such as amino acid and peptide.[13] Because of the high sensitivity of

properties to the number of atoms, the thiolate-protected Au NCs are usually described using the chemical formula $[Au_n(SR)_m]^q$.[54–76] In this formula, *n* is the number of Au atoms, *m* is the number of thiolate ligands (SR), and *q* is the total valence charge on the cluster.

### 1.3.2 Synthesis of thiolate-protected gold nanoclusters

The synthesis of Au NCs has been widely studied over the last few decades. Initially, gas phase metal clusters were reported.[77] However, the gas state metal clusters were short-lived and hard to functionalize. Solution-phase synthesis helped Au NCs to achieve better stability.[77] Since the well-established synthesis protocol of thiolate-protected Au NPs by Brust *et al.*,[78,79] the synthesis of Au NCs has generally included two routes: "atoms to clusters" and "clusters to clusters".[80] In the route of "atoms to clusters", Au ions are reduced into zerovalent atoms. After that, Au NCs form through nucleation of Au atoms. However, Au NCs easily aggregate to form larger Au NPs. To solve this problem, different types of ligands are employed to stabilize and protect Au NCs. In the other route ("clusters to clusters"), Au NCs are formed by etching surface atoms of other Au NCs with appropriate ligands.[80] To generate thiolate-protected Au NCs using this method, the surface-stablized Au NCs and excessive etchant molecules are mixed. The surface of Au NCs is etched via ligand-exchange. The etchant-Au complexation is then treated under specific conditions including desired temperature and reaction time to reorganize the core and surface structure of the NCs. Finally, Au

NCs with specific composition are purified and collected.

Regarding the synthesis of FCC-like Au NCs, the "clusters to clusters" route was employed to synthesize the $Au_{20}(SR)_{16}$, $Au_{28}(SR)_{20}$ and $Au_{36}(SR)_{24}$ NCs.[73,75,76] In the synthetic process, precursors reacted with excess thiol ligands at specific temperature to form Au NCs with specific composition. For example, $Au_{28}(SR)_{20}$ NCs were prepared from the reaction between excess thiol ligands and $Au_{25}(SR)_{18}^{-}$ precursor at 80 °C for 2 hours.[73] $Au_{20}(SR)_{16}$ NCs were also generated from $Au_{25}(SR)_{18}^{-}$ precursor. In this synthetic process, the precursor reacted with excess thiol ligands at 40 °C for 8 hours.[75] Using a similar method, $Au_{36}(SR)_{24}$ NCs were prepared from the reaction between excess thiol ligands and $Au_{38}(SR)_{24}$ precursor at 80 °C for more than 12 hours.[76] Unlike the above FCC-like Au NCs, the $Au_{44}(SR)_{28}$ NCs were synthesized using both routes via a two-step "size focusing" process.[66] In the first step, size-mixed $Au_x(SR)_y$ NCs were formed from $HAuCl_4$ precursor (*i.e.* atoms to clusters). In the second step, size-mixed NCs were dissolved in toluene and etchant thiol ligands. After reacting at 60 °C for 24 hours, $Au_{44}(SR)_{28}$ NCs were produced in high yield. In the end, $Au_{44}(SR)_{28}$ NCs could be separated from the reaction mixture and collected.

### 1.3.3 Atomic structures of thiolate-protected gold nanoclusters

In 2007, the high purity synthesis and total structure determination of $Au_{102}(SR)_{44}$ was published.[71] It was the first report of the total structure of thiolate-protected Au NCs.[71] Figure 1-1 shows the structural model of $Au_{102}(SR)_{44}$ (all the

models in this thesis were generated after publication). The $Au_{102}(SR)_{44}$ NCs consist of a 79-atom core ($Au_{79}$) core protected by 19 single and two double Au-thiolate staple-like motif.

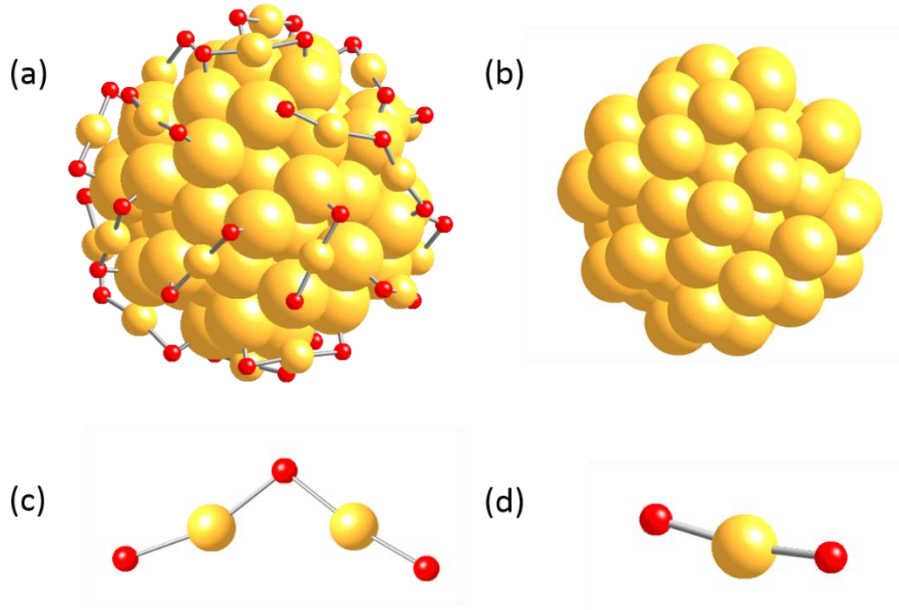


**Figure 1 - 1. (a) Model of the $Au_{102}(SR)_{44}$ NC.[71] $Au_{102}(SR)_{44}$ consists of (b) Au core, (c) double and (d) single staple binding motifs. Yellow represents gold, red represents sulfur atoms. The carbon and hydrogen atoms have been removed for clarity.**

In thiolate-protected Au NCs, types of Au bonding environments can be typically divided into three sites: the core site, the surface site and the staple site. In the core site, these Au atoms only bind to other Au atoms. So, the core has the highest degree of Au-Au coordination. Au atoms in surface sites usually coordinate to both neighboring Au atoms and S atoms from protecting ligands. In the staple site, each Au binds to two S atoms to form the protecting layers for the NCs.

The size of thiolate-protected Au NCs can be precisely controlled. (Figure 1-2)

Size-controlled thiolate-protected Au NCs are found to have different core structures such as the icosahedral Au core, the FCC-like Au core and the smaller Au core (less than the smallest icosahedron of 13 Au atoms) structures. Some of the reported Au NCs are shown in Figure 1-2. Au NCs with an icosahedral Au core structure include $Au_{102}(SR)_{44}$, $Au_{38}(SR)_{24}$ and $Au_{25}(SR)_{18}$ NCs.[71,72,74] (Figure 1-2a, b and c) Smaller than 13-atom Au core structures appear in $Au_{24}(SR)_{20}$ and $[Au_{23}(SR)_{16}]^-$ (Figure 1-2d and e).[52,53]

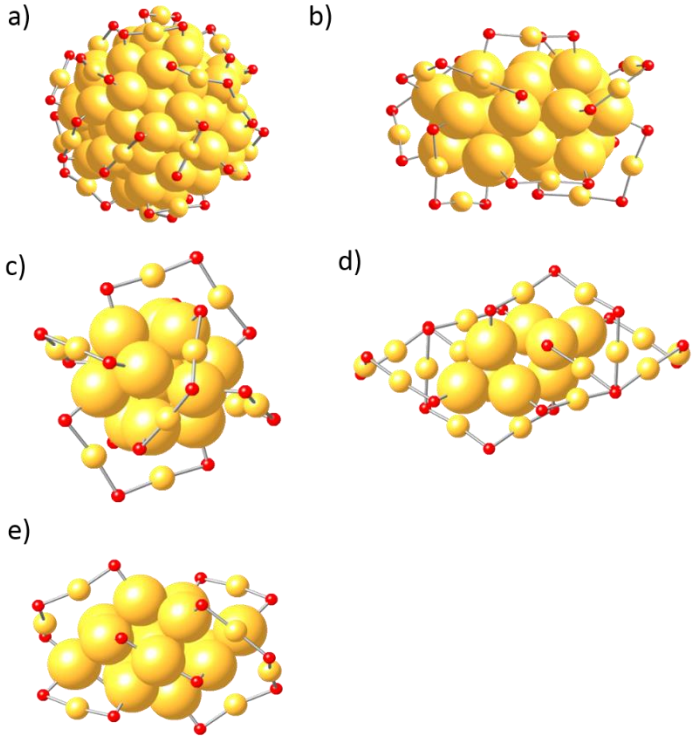


**Figure 1 - 2. Icosahedral type Au NCs: a) $Au_{102}(SR)_{44}$;[71] b) $Au_{38}(SR)_{24}$;[72] c) $Au_{25}(SR)_{18}$.[74] Small or miscellaneous Au core: d) $Au_{24}(SR)_{20}$;[70] e) $[Au_{23}(SR)_{16}]^-$.[67] Carbon and hydrogen are removed for clarity.**

On the surface of Au core, the stabilizing surface structures (*i.e.* the staple-like

motif) have a significant effect on the NC electronic properties due to the strong interaction between gold and sulfur atoms. Various surface staple binding motifs have been identified for Au NCs including single staple, double staple and ring-like staple binding motifs.[13,66,71,75,81,82] Ring-like staple binding motifs refer to the Au-thiolate oligomers with three or more Au atoms. Usually, this type of staple bind motifs only appears in Au NCs with smaller core structures.[75] In contrast, the single and double staple binding motifs are more common in bigger Au NCs.[81,83]

### 1.3.4 FCC-, HCP- and BCC-like thiolate-protected gold nanoclusters

In the past few years, a series of thiolate-protected Au NCs with FCC-like core geometry were reported.[66,73,75,76] This "magic series" can be described using a unified formula of $Au_{8n+4}(SR)_{4n+8}$ (n=2-6) ,[66] such as $Au_{28}(SR)_{20}$, $Au_{36}(SR)_{24}$ and $Au_{44}(SR)_{28}$.[66,73,75,76] $Au_{28}(SR)_{20}$ (Figure 1-3a) consists of a 20-atom ($Au_{20}$) core, four double staple binding motifs and eight bridging S atoms. The bridging S refers to a sulfur atom which connects to two surface Au atoms (Figure 1-3d). $Au_{36}(SR)_{24}$ (Figure 1-3b) consists of a 28-atom ($Au_{28}$) core stabilized by four double staple binding motifs and 12 bridging S atoms. In Figure 1-3c, $Au_{44}(SR)_{28}$ consists of a 34-atom ($Au_{34}$) core, two single staple motifs, four double staple motifs, and twelve bridging S atoms. In all these FCC-like cores, the smallest structural unit with metallic bonds (R<2.88 angstrom) is a four-atom Au ($Au_4$ unit) tetrahedron (Figure 1-3e). These small $Au_4$ units are connected by sharing the vertex Au or longer

distance non-metallic Au-Au bonds (Figure 1-3f).

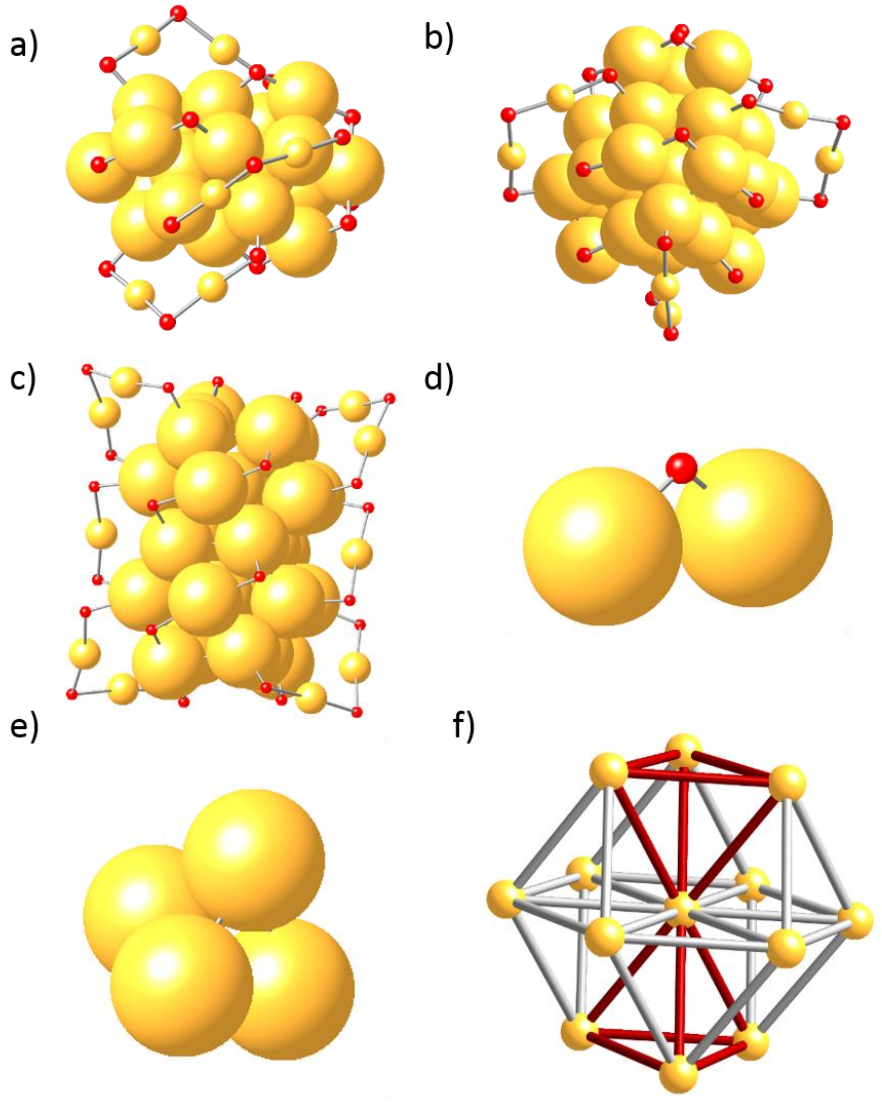


**Figure 1 - 3. FCC type Au NCs: a) $Au_{28}(SR)_{20}$,[73] b) $Au_{36}(SR)_{24}$,[76] c) $Au_{44}(SR)_{28}$.[66] d) A bridging S which connects to two surface Au atoms. e) Smallest structural $Au_4$ unit. f) A $Au_7$ unit core (Au atoms with red bonds) within one-complete-shell FCC cluster.**

In this work, XAS studies of $Au_{44}(SR)_{28}$ will be carried out by comparing them with other previously studied FCC-like NCs such as $Au_{28}(SR)_{20}$ and $Au_{36}(SR)_{24}$. This will help to understand the similarity and difference of local structure and electronic

properties in the FCC-like Au NCs with various sizes. The detailed study of $Au_{44}(SR)_{28}$ is presented in Chapter 3.

Recently, hexagonal-close-packed (HCP)-like $Au_{30}(SR)_{18}$ and body centered cubic (BCC)-like $Au_{38}S_2(SR)_{20}$ were synthesized.[84,85] The HCP- and BCC-like core geometry has never been found in thiolate-protected Au NCs before. The corresponding total structure are displayed in Figure 1-4. $Au_{30}(SR)_{18}$ consists of HCP-like $Au_{18}$ core protected by six dimeric $Au_2(SR)_3$ staple motifs. $Au_{38}S_2(SR)_{20}$ shows a $Au_{30}$ body centered cubic (BCC)-like core stabilized by 4 $Au_2(SR)_3$ staple like motifs. It is interesting to note that the two sulfide atoms in $Au_{38}S_2(SR)_{20}$ has been found for the first time in thiolate-protected Au NCs. The detailed studies of $Au_{30}(SR)_{18}$ and $Au_{38}S_2(SR)_{20}$ are presented in Chapter 4 and 5, respectively.

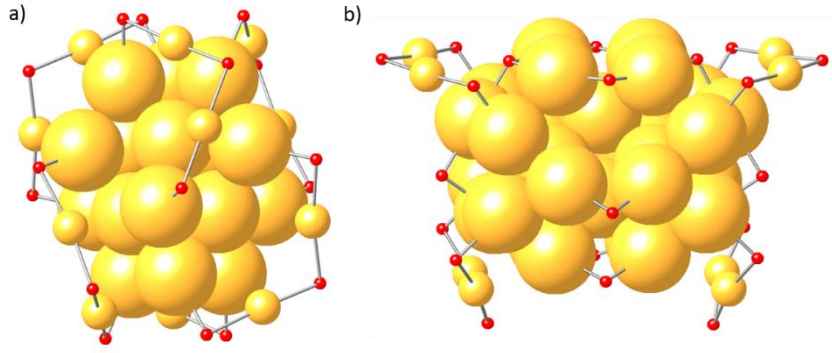


**Figure 1 - 4. Total structure of a) HCP-like $Au_{30}(SR)_{18}$ and b) BCC-like $Au_{38}S_2(SR)_{20}$.**

## 1.4 Motivation and Outline of Thesis

Previous relevant studies of FCC-like Au NCs focused on the comparison of $Au_{28}(SR)_{20}$ and $Au_{36}(SR)_{24}$ NCs with their icosahedral-like counterparts like

$Au_{25}(SR)_{18}$ and $Au_{38}(SR)_{24}$.[81,82] These studies help to understand how their special local structure and electronic properties are influenced by the FCC-like core geometry. These studies implied that how these FCC-like Au NCs are related to their icosahedral-like counterparts regarding the structure and bonding properties. More recently, a few new FCC-like Au NCs have been reported such as $Au_{20}(SR)_{16}$[75] and $Au_{44}(SR)_{28}$.[66] In this thesis, the study of FCC-like Au NCs will focus on $Au_{44}(SR)_{28}$ NCs. They were compared to the other FCC-like NCs with a goal to understand the overall trend in their structural and bonding properties. Furthermore, HCP-like and BCC-like Au NCs cannot be studied using the same method as FCC-like Au NCs because only one cluster has been found so far for each category. Therefore, HCP-like $Au_{30}(SR)_{18}$ is compared with icosahedral and FCC-like Au NCs to study the bonding properties related to the core geometry. Different from HCP-like Au NCs, the research of BCC-like $Au_{38}S_2(SR)_{20}$ is carried out together with Au NCs which has similar component and NC size.

Following the introduction, Chapter 2 presents the experimental details. First, synchrotron radiation and facilities used to collect EXAFS data are discussed. Next, principles of X-ray absorption spectroscopy are presented. The general theoretical background of extended X-ray absorption fine structure (EXAFS) and X-ray absorption near-edge structure (XANES) is discussed. Furthermore, the *ab initio* calculations of X-ray spectroscopy using the FEFF computer code is introduced.[86]

Au NC with FCC-like core structure, $Au_{44}(SR)_{28}$ is studied in Chapter 3. All the

results and discussion are based on the measurements from the experimental XAS data. Firstly, the local structure of $Au_{44}(SR)_{28}$ is studied using Au $L_3$-edge temperature-dependent EXAFS by comparing it with $Au_{28}(SR)_{20}$ and $Au_{36}(SR)_{24}$. Bond distance distribution of $Au_{44}(SR)_{28}$ was calculated based on the total structure. The coordination numbers (CN) calculated from bond distance distribution are then used in the temperature-dependent EXAFS fit. Based on the fitting results, the negative thermal expansion (NTE) is found in the Au-S, the shorter Au-Au and the longer Au-Au scattering shells in $Au_{44}(SR)_{28}$. Finally, by comparing the temperature-dependent EXAFS fitting results from $Au_{28}(SR)_{20}$ and $Au_{36}(SR)_{24}$, size-dependent NTE is discussed for these NCs.

Next, the study of HCP-like $Au_{30}(SR)_{18}$ is shown in Chapter 4. The bonding properties of $Au_{30}(SR)_{18}$ were probed using XAS measurements and were further compared with icosahedral-like $Au_{25}(SR)_{18}$ and FCC-like $Au_{36}(SR)_{24}$. The analysis of XANES, together with theoretical calculations, is firstly performed to understand the relationship between early region of XANES and Au-Au bond distances in varied gold sites. The Au $L_3$-edge temperature-dependent EXAFS is then carried out to explain the more pronounced NTE in HCP-like gold core.

In Chapter 5, the bonding properties of BCC-like $Au_{38}S_2(SR)_{20}$ are also carried out using XAS measurements. The similar-sized bi-icosahedral $Au_{38}(SR)_{24}$ NC is used as a comparison. Firstly, experimental XANES in association with simulated XANES helps to understand how Au-Au bond distance effect the early region of XANES. The

Au $L_3$-edge EXAFS of $Au_{38}S_2(SR)_{20}$ and $Au_{38}(SR)_{24}$ from solid and solvent phase is then compared to discuss the negative expansion in $Au_{38}S_2(SR)_{20}$ upon solvation.

Finally, the conclusion and future work is discussed in Chapter 6. Conclusion on the $Au_{44}(SR)_{28}$ study is presented from the perspective of local structure and the size-dependent NTE trend. The finding of the near-edge XANES and NTE of $Au_{30}(SR)_{18}$ is summarized. Furthermore, the study of $Au_{38}S_2(SR)_{20}$ is concluded with XANES and Au-Au bond expansion upon solvation. In the end, future work for this thesis is proposed, which includes adding the new $Au_{52}(SR)_{32}$ into the comparative study of FCC-like Au NCs, studying new HCP-like Au NCs and understanding how Au-Au bond distance expansion upon solvation happens in $Au_{38}S_2(SR)_{20}$.

# Chapter 2 – Experimental Techniques

## 2.1 Introduction to Synchrotron Radiation

Synchrotron radiation is the electromagnetic radiation emitted by charged particles travelling on a curved trajectory.[87] It is a very powerful tool which can provide intense photon flux with tunable wavelengths ranging from infrared light to hard X-rays.[87] In a modern synchrotron facility (Figure 2-1), the electrons are first accelerated in a linear accelerator. Accelerated electrons are injected into a booster ring to achieve near-relativistic speeds (*i.e.* near light speed). These electrons are then injected into the storage ring. In the storage ring, the electrons can be controlled by the magnetic fields to travel on a desired trajectory. When the electrons pass through the bending magnets and/or insertion devices (undulators, wigglers), synchrotron radiation is produced. Finally, the generated electromagnetic radiation is delivered to the different beamline stations.

In a third-generation synchrotron facility, three types of magnets are commonly employed including bending magnets, undulators and wigglers. Bending magnets can help to produce a curved trajectory of the charged particles. Wigglers provide stronger magnetic fields and cause a broader electron beam with higher beam intensity than bending magnets. Different from wigglers, undulators with relatively weaker magnetic fields usually help to give a narrower photon beam with a smaller range of energy and

a much higher beam intensity.[87]

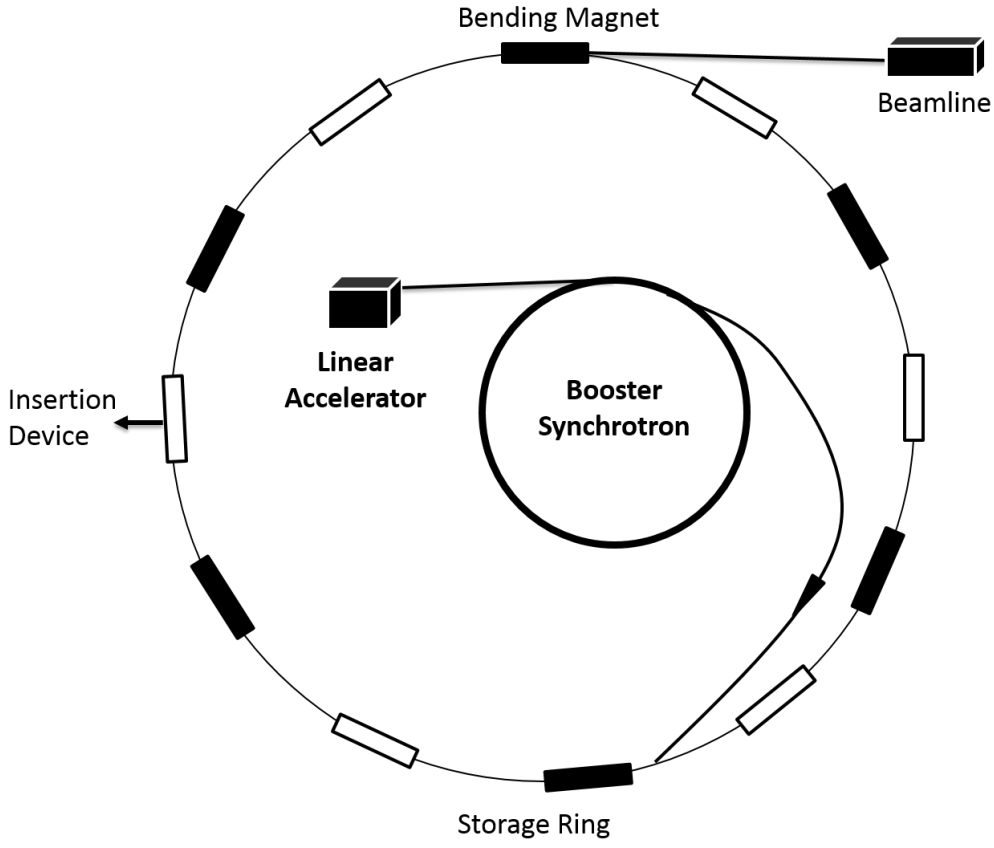


**Figure 2 - 1. A general schematic for a synchrotron facility.**

Based on the energy range needed for specific experiments, different synchrotrons and/or beamline stations are selected for radiation-based measurements. The Advanced Photon Source (APS) was used in this work. The APS is located at Argonne National Laboratory and is one of the U.S. synchrotron facilities which is available since 1995. The APS has a storage ring with very high energy and thus is particularly suitable for hard X-ray experiments. The APS consists of 34 sectors with 70 beamlines in total. Each sector contains one or more beamlines. Although the energy range of the beamlines is quite broad at the APS, X-ray beams with more intense photon flux can

often be achieved in the hard X-ray region than a smaller synchrotron. Therefore, it is more desirable to measure heavy elements with higher binding energies.

The hard X-ray measurements presented in this thesis were conducted at Sector 20 of the APS. The bending magnet beamline at sector 20 (20-BM-B) has an energy range of 2.7-32 keV and can be employed for the measurements of XAFS and Microfluorescence (hard X-ray). In this study, Au $L_3$-edge XANES/EXAFS experiments were carried out at this beamline.

## 2.2 X-ray Absorption Spectroscopy (XAS) Technique

### 2.2.1 Introduction to X-ray absorption and detection

X-ray absorption spectroscopy (XAS), also called X-ray absorption fine structure (XAFS), is a widely used technique to determine the bonding structure and electronic properties for various materials.[13] XAS is one of the few structural tools which can be used to study noncrystalline and highly disordered materials, including those in solution phase. Because of its element specific feature, XAS is particularly useful for the measurement of multi-element samples. In addition, due to the use of synchrotron facility, XAS shows a high sensitivity in the measurements. This makes XAS widely used for nanomaterials of small quantity.

In a typical transmission XAS measurement, an X-ray beam passes through a sample and the change of X-ray beam intensity will be monitored. In the measurement,

X-ray absorption will occur only if the incident photon has sufficient energy to promote the core-electrons to higher unoccupied states (Figure 2-2). Such an absorption induces a sudden increase in the absorbance, which is referred to as an absorption edge (e.g. K, $L_1$, $L_2$, $L_3$, $M_1$ edge *etc*.). The commonly used absorption edges and corresponding electronic transitions are listed in Table 2-1. Therefore, the X-ray excitation energies of the absorption edges are equal to the binding energies (unique in each element) of the core-electrons being excited. This also explains the element-specific nature of the XAS measurements.

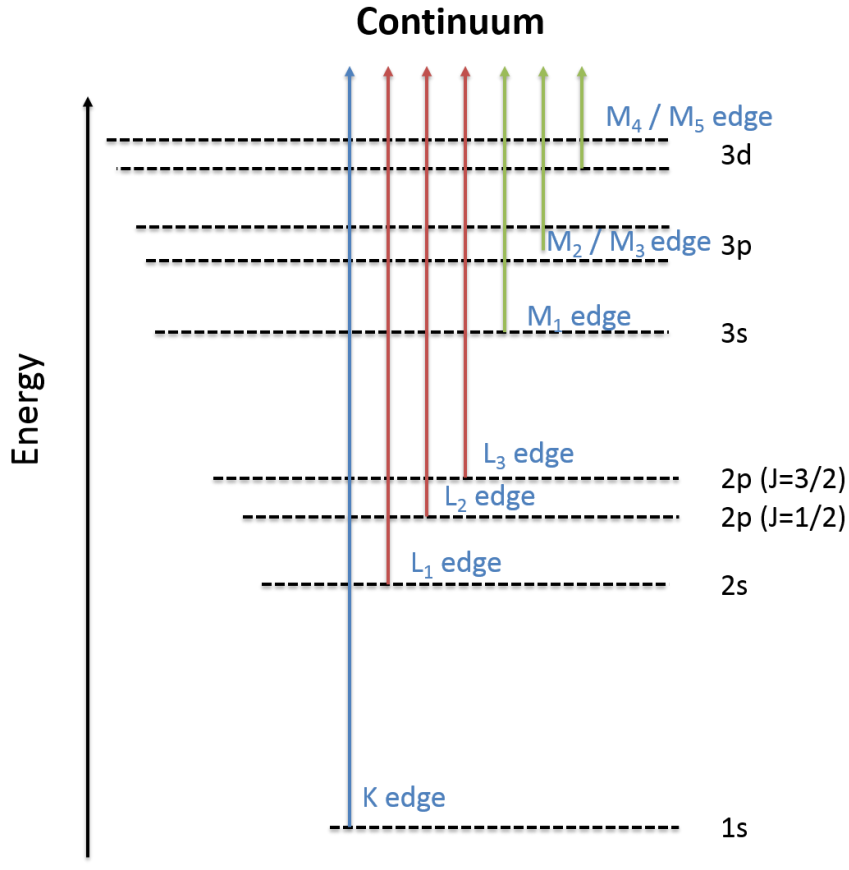


**Figure 2 - 2. Three major transitions: K edge, L edge and M edge transitions are identified.**

**Table 2 - 1. Absorption edges and the different transitions between initial states and final states.**

| Absorption edge | Initial state | Final state |
|---|---|---|
| K state | 1s | p |
| $L_1$ state | 2s | p |
| $L_2$ state | $2p_{1/2}$ | s, d |
| $L_3$ state | $2p_{3/2}$ | s, d |
| $M_1$ state | 3s | p |
| $M_2$ state | $3p_{1/2}$ | s, d |
| $M_3$ state | $3p_{3/2}$ | s, d |

The electronic transitions listed in table 2-1 observe the following dipole selection rule:

$$\Delta l = \pm l \quad (1)$$

where $\Delta l$ represents the difference of angular momentum quantum number between initial and final electronic states. For instance, the most studied K- and $L_3$-edges for NPs represents the transitions from 1s to valence p-state and from 2p to valence d-states, respectively.

Due to the absorption, the intensity of transmitted X-rays will be decreased. The decrement can be quantified by using the intensity of the X-ray beam before ($I_0$) and after transmission ($I$) through the sample. In X-ray transmission, $\mu(E)$ can be derived

using equation:

$$\mu(E) = \log(I_0/I) \quad (2)$$

The X-ray absorption coefficient ($\mu(E)$) is dependent on atomic number and the incident X-ray energy. Regardless of local environment, $\mu$(E) is intrinsic to each element.

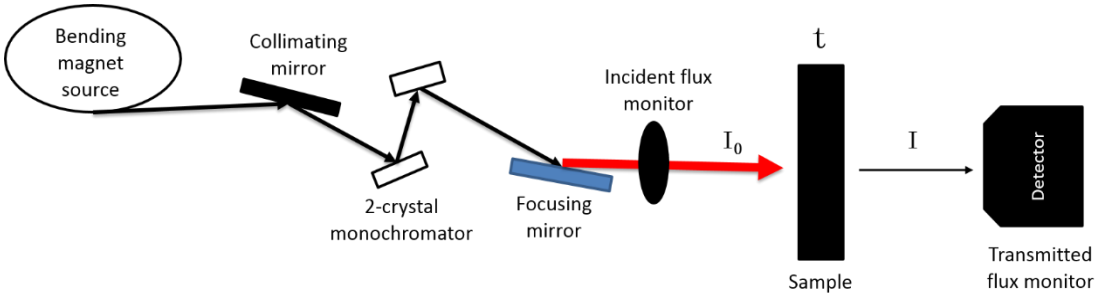


**Figure 2 - 3. Incoming X-ray with intensity of $I_0$ passed through the sample of thickness t. the transmitted X-ray beam has intensity of I.**

The absorption coefficient ($\mu(E)$) can also be derived from the X-ray fluorescence. In X-ray fluorescence, the electron in the higher energy level fills the core hole and ejects an X-ray photon with well-defined energy (Figure 2-4a). The ejected photon will finally be detected by an X-ray fluorescence detector (Figure 2-4b). Therefore, the relationship between energy and absorption coefficient is described using the equation:

$$\mu(E) \propto I_f / I_0 \quad (3)$$

where $I_f$ is the intensity of and $I_0$ is the intensity of incident X-rays.

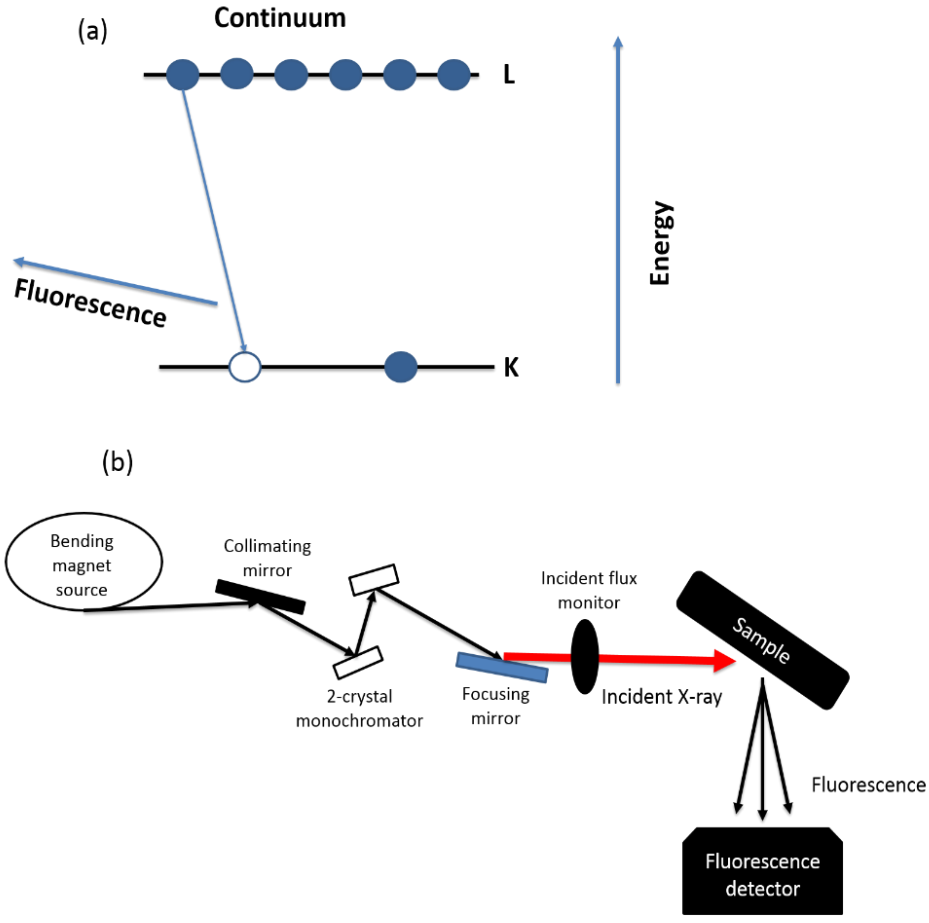


**Figure 2 - 4. (a) X-ray fluorescence, (b) Schematic view of X-ray fluorescence from a material. Fluorescence is collected by fluorescence detector on the bottom which is at an appropriate angle with the sample.**

In experiments, samples in different phases usually have different thickness and concentrations. When the sample with high concentration is uniform and free of pinholes, the X-ray transmission mode is usually employed. On the contrary, X-ray fluorescence mode is the preferred technique for the low concentration samples. If high concentration samples are measured using fluorescence mode, the ejected fluorescence photons will be self-absorbed by the samples. This self-absorption will influence the accuracy of the XAS measurement.[88]

The absorption coefficient $\mu(E)$ measured near and above the absorption edge of element is plotted against X-ray energy to form the XAS spectrum. The complete XAS spectrum can be broken into two main portions: X-ray absorption near-edge spectroscopy (XANES) and extended X-ray absorption fine structure (EXAFS).[89] The XAS spectrum of Au foil is used as an example (Figure 2-5). In the total spectrum, the early region of the spectrum is normally called XANES. The EXAFS part is the oscillation in the later region. XANES is widely used to study electronic properties. EXAFS is employed to study structural information including bond distance (R) and CN. The principles of XANES and EXAFS will be discussed separately below.

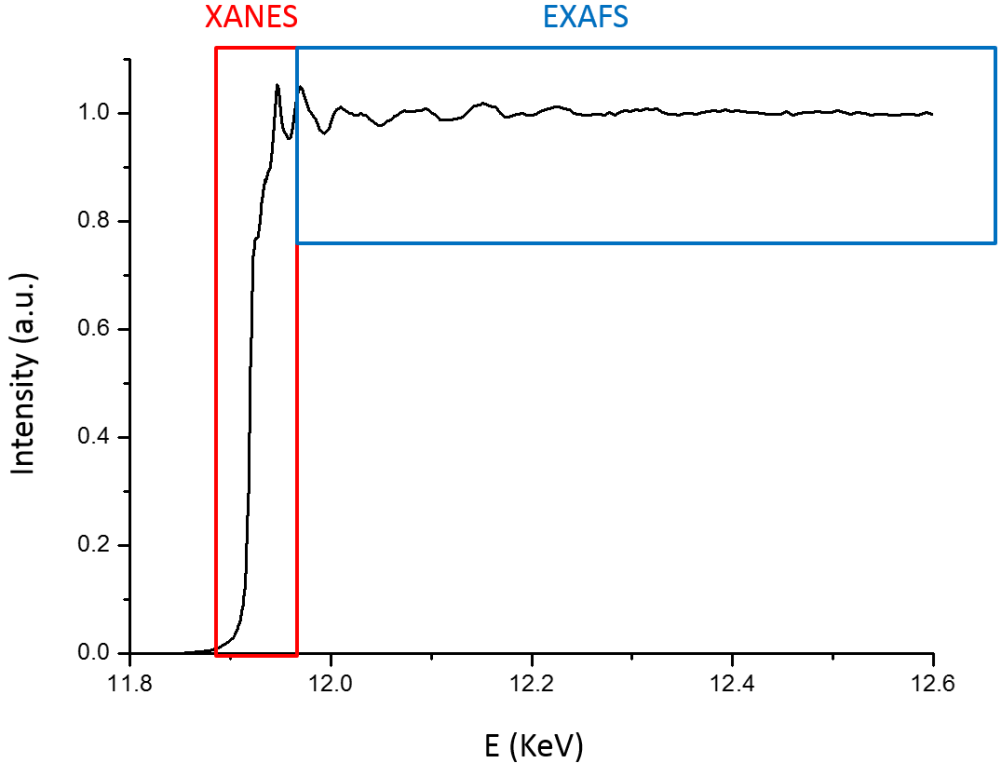


**Figure 2 - 5. XAFS for Au foil. The measured spectrum is shown with the XANES and EXAFS regions identified.**

### 2.2.2 X-ray absorption near-edge spectroscopy (XANES)

The XANES region of an XAS spectrum typically ranges from ± 30 eV from the absorption edge. It can be divided into the pre-edge, absorption edge and post-edge sections (Figure 2-6). The section with weak intensity and lower energy than the absorption edge is referred to as the pre-edge XANES (Figure 2-6①). It is the only section in XANES which sometimes has no direct physical meaning for certain elements like heavy metals. For example, pre-edge features do not occur in Ag K-edge and Au $L_3$-edge XANES of NPs.[82,90] However, the physical meaning of pre-edge is significant for elements with low atomic number. For instance, small pre-edge features were found in S K-edge XANES spectra of thiolate-protected metal NPs, which are useful to probe ligand-metal bonding.[90] Furthermore, the pre-edge section plays an important role in data processing (i.e. normalization) of XAS spectra.

The most significant change of absorbance in the XANES spectrum takes place at the absorption edge (Figure 2-6②), which arises from transitions of electrons between occupied core states to unoccupied valence states. Because of the transitions of electrons, absorption edge is sensitive to the effective nuclear charge. That is why absorption edge can help to study the electronic properties such as oxidation state. For example, if K-edge transitions are compared for metal and metal oxides of the same element, the energy required for metal oxides is higher because of the high effective nuclear charge. Then the difference in the absorption edge position can help

to distinguish the oxidation states.

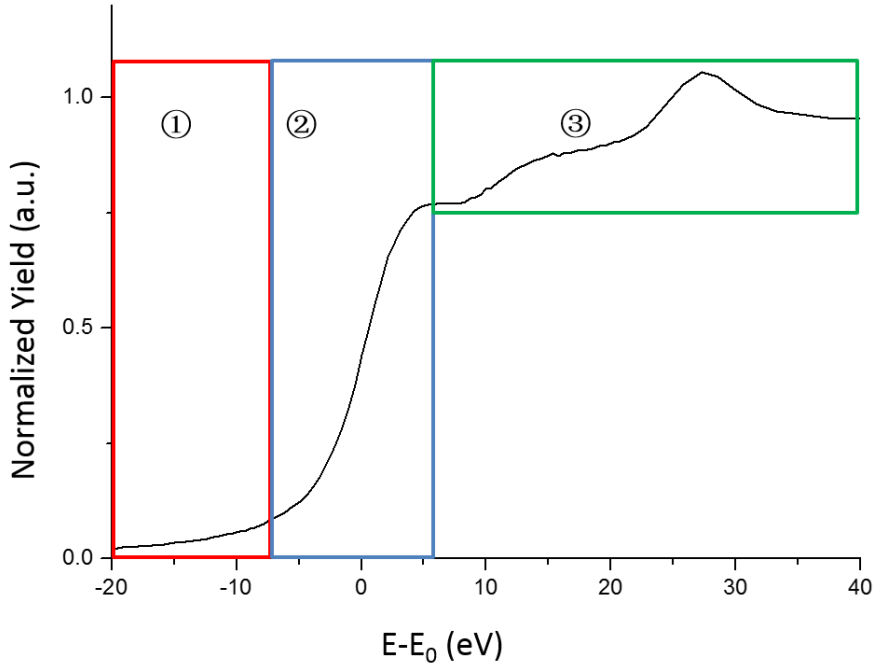


**Figure 2 - 6. Au $L_3$-edge XANES spectrum of Au foil showing the ① pre-edge ② absorption edge and ③ post-edge sections.**

The post-edge section (Figure 2-6③) is attributed to two effects. The first one is the electronic transition between energy states. However, these transitions sometime do not follow the dipole selection rule. For instance, the post-edge feature caused by the electronic transitions between *s* states and *d* states is found in S K-edge XANES of Au NCs.[81] The second effect is the scattering of photoelectrons between multiple neighboring atoms. In this case, emitted photoelectrons travel in all directions, with some scattered photoelectrons returning to the absorbing atom. Because the photoelectrons can be scattered by multiple atoms, various scattering paths such as the triangular and linear multiple scattering paths (Figure 2-7① and ②) contribute to the

spectral oscillations immediately following the absorption edge. Different oscillation features can provide qualitative information about the structure around the absorbing atom, such as lattice type.

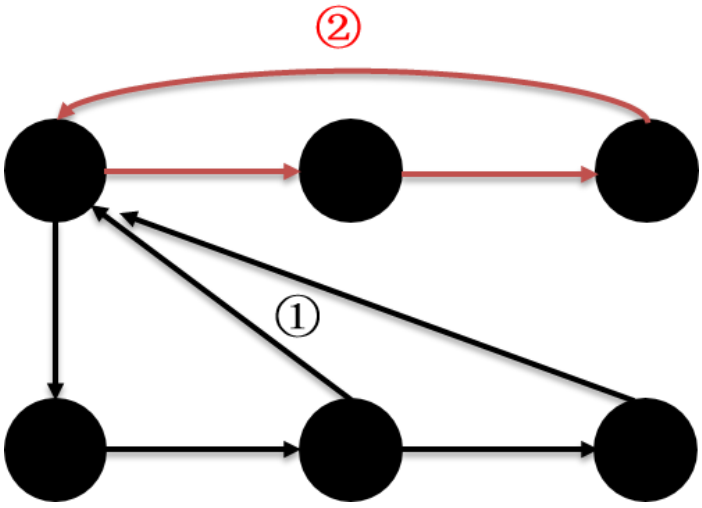


**Figure 2 - 7. Multiple scattering paths: ① triangular and ② linear multiple scattering paths contribute to post-edge in XANES spectrum.**

### 2.2.3 Extended X-ray absorption fine structure (EXAFS)

Oscillations related to the EXAFS region begin approximately 30 eV after the absorption edge. The origin of these post-edge oscillations can be explained in several key steps. In the first step, the X-ray beam with high enough energy excites core electrons from absorbing atom. The excitation of core electrons from lower energy level to the vacuum level produces the photoelectron wave. The photoelectron wave then reaches the neighboring atoms (Figure 2-8a). In the second step, the outgoing photoelectron wave interacts with the neighboring atoms to produce a backscattered

photoelectron wave that travels back towards the original absorbing atom (Figure 2-8b). The phase and amplitude of the backscattered photoelectron depend on parameters such as the energy of the emitted photoelectron wave and atomic number of the backscattering atoms. The interaction of the original and backscattered photoelectron waves will alter the absorption coefficient. If the backscattered photoelectron wave is in phase with the original photoelectron wave, the absorption coefficient will increase. If the backscattered photoelectron wave is out of phase, the absorption coefficient will decrease. The increase and decrease in the absorbance over the course of the XAS measurement will result in the observed EXAFS oscillations.

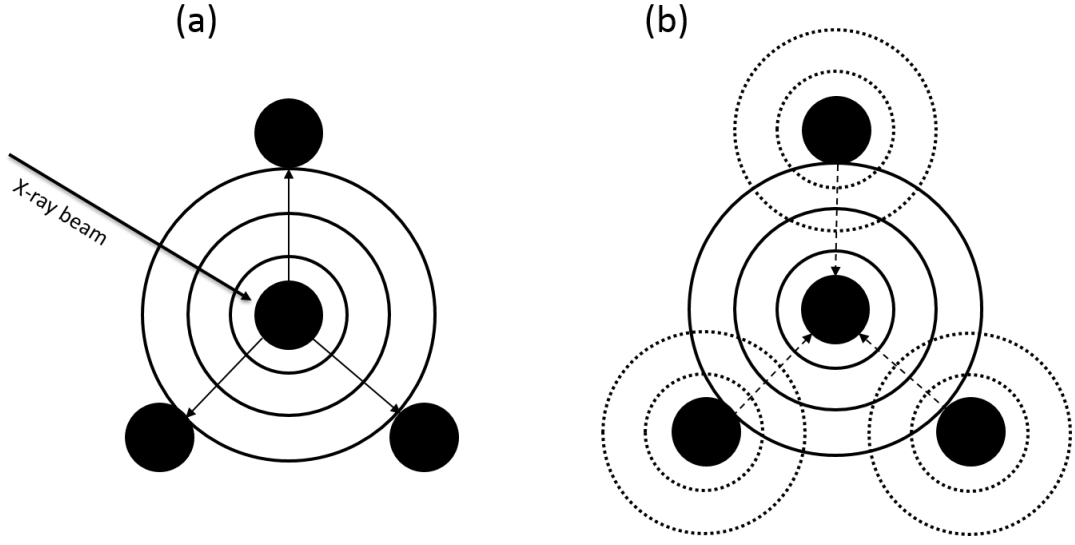


**Figure 2 - 8. Schematic view of photoelectron scattering. The steps involved include (a) absorption of X-ray photon, emission of photoelectron wave and (b) backscattered photoelectron wave from neighboring atoms.**

The measured EXAFS signal, $\chi(E)$, is described by:

$$\chi(E) = \frac{\mu(E) - \mu_0(E)}{\Delta\mu_0(E)} \quad (4)$$

where $\mu(E)$ is the measured absorption coefficient, and $\mu_0(E)$ is a smooth background function representing the absorption of an isolated atom. $\Delta\mu_0(E)$ is the measured change in the absorption $\mu(E)$ after the absorption edge. Isolated $\chi(E)$ is generated by the normalized XAS spectrum (Figure 2-9a). Furthermore, the EXAFS oscillations in $\chi(E)$ are often described in terms of the photoelectron wavenumber, *k*:

$$k = \sqrt{\frac{2m(E - E_0)}{\hbar^2}} \tag{5}$$

where $m$ is the mass of an electron, $E$ the incident X-ray photon energy, $E_0$ the absorption edge energy, and $\hbar$ the reduced Planck's constant. When $\chi(k)$ is plotted to k, the resulted spectrum is referred to as *k*-space EXAFS. The y-axis of *k*-space EXAFS is always weighted by multiplying $\chi(k)$ by $k^x$ (where *x* equals 1, 2 or 3 typically) to account for the decay of oscillations with increasing energy or k.[91] For example, the oscillations in the late region of k-space spectrum from Au foil $L_3$-edge are very weak if $\chi(k)$ is multiplied by $k^0$ (Figure 2-9b). When the $\chi(k)$ is multiplied by $k^3$ (Figure 2-9c), these oscillations are more clearly displayed.

The various frequencies in the oscillations in $\chi(k)$ correlate to the near-neighbor coordination shells around the absorbing atom which can be isolated via Fourier transformation. The Fourier-transformed EXAFS spectrum is sometimes called R-space (Figure 2-9d). R-space EXAFS is useful to study the local bonding environment, wherein the position and intensity of the peak are determined by the bond distance and CN. However, the bond distance herein is not the actual bond length because of phase

shifting.

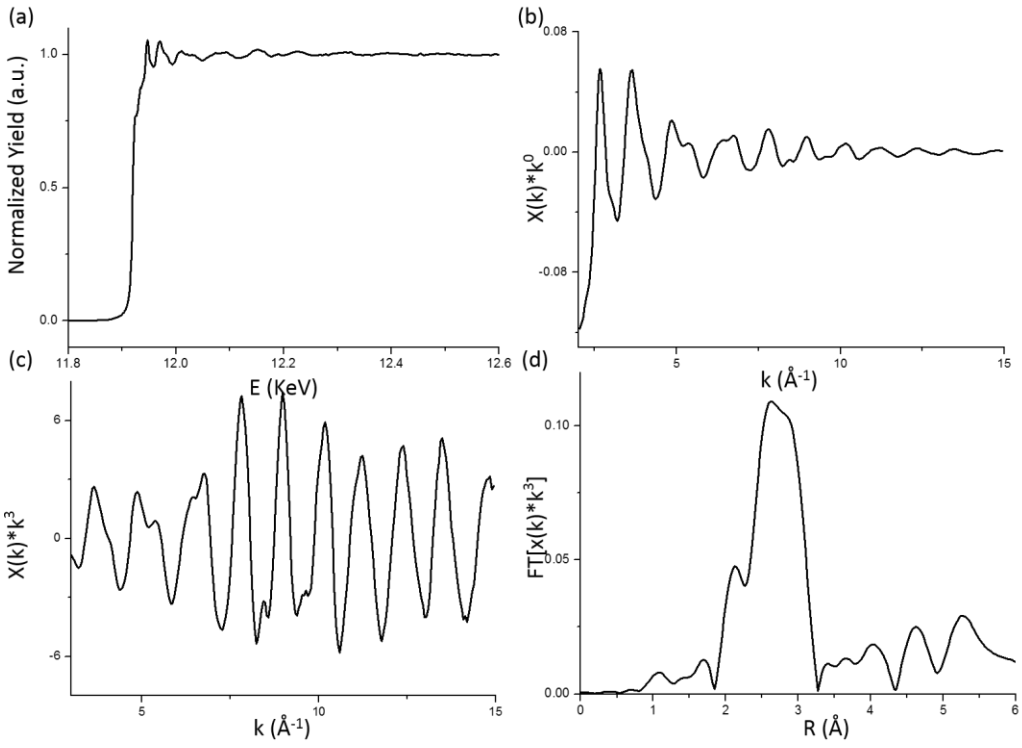


**Figure 2 - 9. EXAFS data refinement (generated from Au foil). (a) XAS spectrum of Au foil is normalized. The EXAFS is transformed into k-space with (b) $\chi(k)*k^0$ and (c) $\chi(k)*k^3$ weight at the Au $L_3$-edge. In the end, k-space is Fourier-transformed to (d) R-space.**

The bonding environment of the absorbing atom can be described and modeled by using the EXAFS equation:[92,93]

$$\chi(k) = \sum_j \frac{S_0^2 N_j e^{-2k^2\sigma_j^2} e^{-2R_j/e^{\lambda(k)}} f_j(k)}{kR_j^2} \sin[2kR_j + \delta_j(k)] \qquad (6)$$

where $f(k)$ and $\delta(k)$ are the scattering amplitude and the scattering phase shift of the neighboring atoms, respectively. $N$ is the coordination number, R is the distance of the absorbing atom to the neighboring atoms, and $\sigma^2$ is the disorder in the

neighboring atom distance. Furthermore, j represents a particular coordination shell, also known as scattering path, describing identical neighboring atoms at approximately the same distance from the absorbing atom. In addition, $S_0^2$ is the amplitude reduction factor which accounts for intrinsic losses in the X-ray absorption process.

The EXAFS equation is used to determine the structural parameters $N$, R and $\sigma^2$ if $f(k)$ and $\delta(k)$ are known during the EXAFS refining process. To refine the R-space spectrum with the EXAFS equation, the WinXAS computer program is employed in this thesis to analyze these structural parameters.[94] In addition, the energy-shift parameter ($\Delta E_0$) is also included in the refinement to account for the phase differences between experimental and theoretical backscattering paths. The values of $f(k)$ and $\delta(k)$ can be derived from either experimental EXAFS spectra of reference materials or from *ab initio* simulations of appropriate structural models using the FEFF code.[86,95,96]

## 2.3 *Ab Initio* Calculations/Simulations of XAS

FEFF is an *ab initio* self-consistent multiple scattering code. Based on Green's function, it can calculate the backscattering phase amplitudes and phase shifts required for EXAFS analysis.[86,95,96] In order to carry out this calculation, the atomic coordinates of the structure models are provided from a known crystal structure. Furthermore, density functional theory (DFT) structural modeling is another important tool to

provide the atomic coordinates for FEFF calculations. The calculated files for refinement of experimental EXAFS spectra are then produced to study the local structure. Because the absorbing atom can be specifically selected by modifying the input file, the simulation studies of clusters are then very easy to carry out from different atomic sites for the same element. In addition, extra calculations can be added to the simulations by modifying the input file. For instance, the DEBYE function can be included in the input file to calculate Debye-Waller factors for each path.

The electronic structure around the absorbing atom can also be calculated using the FEFF program, although it is not as reliable as DFT calculations for complicated systems. To reduce the computational cost, a number of approximations are made. For example, the electron wave function is replaced by Green's function. In addition, spherically symmetric muffin-tin potentials are used rather than full potentials. This means the atomic potentials stay around an atom with a specific radius and the potential between interstitial atoms remains constant.[88] In electronic studies, the electronic transitions and the multiple scattering excitations can be calculated by FEFF. For instance, the projected local densities of states (l-DOS) simulations can be conducted by adding the l-DOS card in the input file, and such information will help explain occupancy of an energy state which further help to generate XANES.[89,97]

# Chapter 3 – Face-Centered Cubic (FCC)-like $Au_{44}(SR)_{28}$

*Sections 3.2-3.4 are reproduced in part with permission from*: Yang, R.; Chevrier, D. M.; Zeng, C.; Jin, R.; Zhang, P. Bonding properties of FCC-like $Au_{44}(SR)_{28}$ clusters from X-ray absorption spectroscopy. *Can J. Chem.* **2017**, *95*, 1220-1224. Copyright 2017, NRC Research Press.

## Contributions

C.Z. synthesized the $Au_{28}(SR)_{20}$, $Au_{36}(SR)_{24}$ $Au_{44}(SR)_{28}$ NCs. D.M.C. carried out the Au $L_3$-edge XAS measurements at the Sector20-BM beamline of the Advanced Photon Source (Argonne National Laboratory, IL, U.S.A.). R.Y. performed the data analysis, conducted *ab initio* calculations, and wrote the manuscript. P.Z. supervised R.Y. and helped with manuscript revision.

## 3.1 Introduction

FCC-like Au NCs attract significant amount of interest because these ultrasmall particles exhibit unexpected core structure of FCC geometry, similar to the bulk gold. The reported $Au_{44}(SR)_{28}$ ($Au_{44}$ for short) is one of the thiolate-protected Au NCs with a FCC-like core structure in the FCC-like series including the well-studied $Au_{28}(SR)_{20}$ ($Au_{28}$ for short) and $Au_{36}(SR)_{24}$ ($Au_{36}$ for short).[66,73,76] In the research of Au NCs, XAS has been found useful to probe the bonding properties of these Au NCs.[48] For instance, the unique structural and electronic properties were found in $Au_{28}$ and $Au_{36}$ NCs by comparing with icosahedral Au NCs, where the small tetrahedral $Au_4$ unit within the

gold cores play a very important role in controlling their bonding and electronic properties.[81,82] Furthermore, based on the results from temperature-dependent X-ray absorption spectroscopy (XAS) experiments, it is interesting to note that a negative thermal expansion was found in the first Au-Au shell in $Au_{36}$, but not in $Au_{28}$ NCs.[81,82] However, such studies only focus on individual Au NCs by comparing the FCC with icosahedral counterpart. The overall trend of size-dependent bonding in FCC-like "magic series" from XAS perspective was still unavailable with only two Au NCs ($Au_{28}$ and $Au_{36}$).

In this work, we have compared the recently discovered $Au_{44}$ with the other two Au NCs ($Au_{28}$ and $Au_{36}$). Based on a multi-shell EXAFS fitting analysis and temperature-dependent XAS measurements, the size-dependent bonding behavior of these NCs is discussed herein. This work, together with our previous studies, highlights the bonding trend in the FCC-like magic series.

## 3.2 Experimental Methods

### 3.2.1 Synthesis of $Au_{28}$, $Au_{36}$ and $Au_{44}$

The synthesis of $Au_{28}$, $Au_{36}$ and $Au_{44}$ NCs were conducted at Carnegie Melon University. In detail, $Au_{28}$ NCs were prepared from the reaction between excess thiol ligands and $Au_{25}$-precursor at 80 °C for 2 hours.[66] Using a similar method, the $Au_{36}$

NCs were prepared from the reaction between excess thiol ligands and $Au_{38}$ precursor at 80 °C for more than 12 hours. Unlike the above FCC-like Au NCs, the $Au_{44}$ NCs were synthesized using both routes via a two-step "size focusing" process. In the first step, size-mixed $Au_x(SR)_y$ NCs were formed from $HAuCl_4$ precursor (i.e. atoms to clusters). In the second step, the size-mixed NCs were dissolved in toluene and etchant thiol ligands. After reacting at 60 °C for 24 hours, $Au_{44}$ NCs were produced in high field. All the syntheses produced Au NCs in high purity which is supported by mass spectrometer data.

### 3.2.2 X-ray absorption spectroscopy (XAS)

The Au $L_3$-edge XAS measurements of $Au_{44}$ were carried out in transmission mode at the Sector20-BM beamline of the Advanced Photon Source (Argonne National Laboratory, IL, U.S.A.). In the measurement, $Au_{44}$ powder samples were packed into Kapton film pouches, sealed and folded to ensure high quality EXAFS signals are collected. The samples were measured in transmission mode which is represented using log ($I_0$/ $I_1$). A Au foil reference was placed in between the $I_1$ detector and another detector $I_2$ to simultaneously collect the XAFS data for calibration of the energy of Au $L_3$ absorption edge. The XAS data were collected at both low temperature (LT: 90K) using a helium-cooled cryostat chamber and room temperature (RT: 300K) under ambient conditions.

### 3.2.3 Data analysis

The XAS data processing and EXAFS fitting were performed using the WinXAS 3.1 software package[94] and FEFF8.2 computer code.[86,95,96] In the refinement process, the amplitude reduction factor ($S_0^2$) of 0.9 was obtained by fitting the Au foil EXAFS and fixed for the EXAFS fitting of Au NCs. For multishell EXAFS fitting, CN of Au-S and Au-Au shells are fixed based on the published $Au_{44}$ total structure.[66] A k-range of 3-14 $Å^{-1}$ was used for the Fourier transformation and fitting of the EXAFS. All the $E_0$ shift values were correlated to reduce the number of free running parameters, allowing for the incorporation of up to three scattering shells.

## 3.3 Results and Discussion

### 3.3.1 Qualitative XAS comparison

The Au $L_3$-edge XANES of $Au_{28}$, $Au_{36}$ and $Au_{44}$ is first compared in Figure 3-1. Interestingly, when the XANES is closely compared in the overlapped plot in Figure 3-1, identical features are observed for the three NCs in the whole XANES region, including the white line (the first feature following the absorption edge) intensity. These observations imply that their electronic properties are identical and independent of the cluster size. A more detailed discussion on this finding will be presented together with the EXAFS fitting results in the later section.

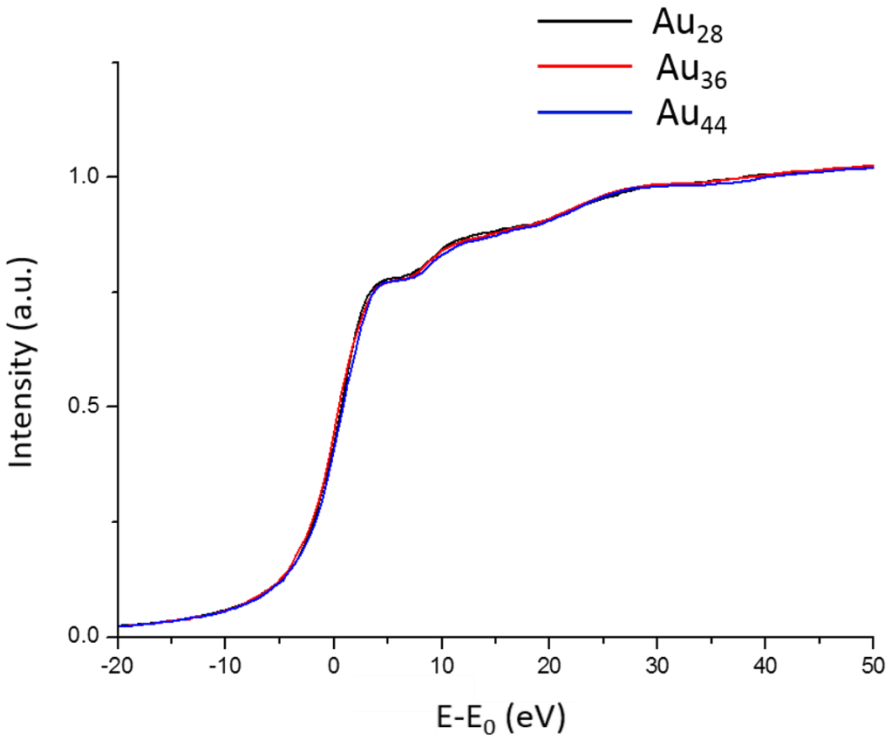


**Figure 3 - 1. Overlapped XANES of $Au_{28}$, $Au_{36}$ and $Au_{44}$.**

The FT-EXAFS spectra of $Au_{28}$, $Au_{36}$ and $Au_{44}$, collected at LT and RT, are plotted in Figure 3-2. The most intense peak around 1.9 Å in each spectrum is caused by the Au-S scattering. The intensity of these peaks decreases when their size increases in both RT and LT series. To understand this trend, we calculated the CN of the Au-S coordination when the NC size increases. The Au-S CN gives a value of 1.43 for $Au_{28}$, 1.33 for $Au_{36}$ and 1.27 for $Au_{44}$. From these calculated CN values, we can understand that the observed trend for these EXAFS peaks is caused by the decrease of Au-S CNs. The small peaks between 2.5 Å and 3.5 Å correspond to the Au-Au scatterings. Similar patterns of the FT-EXAFS of the three Au NCs at LT and RT indicate a similar local structure for these FCC-like Au NCs. In addition, spectra

with lower peak intensity in the Au-Au scattering region are found at RT comparing with the LT data. This is because the thermal vibrations at higher temperature lead to a higher degree of thermal disorder, which reduces the EXAFS scattering intensity. Quantitative information of these scattering shells will be obtained by the refinement of FT-EXAFS in the next section.

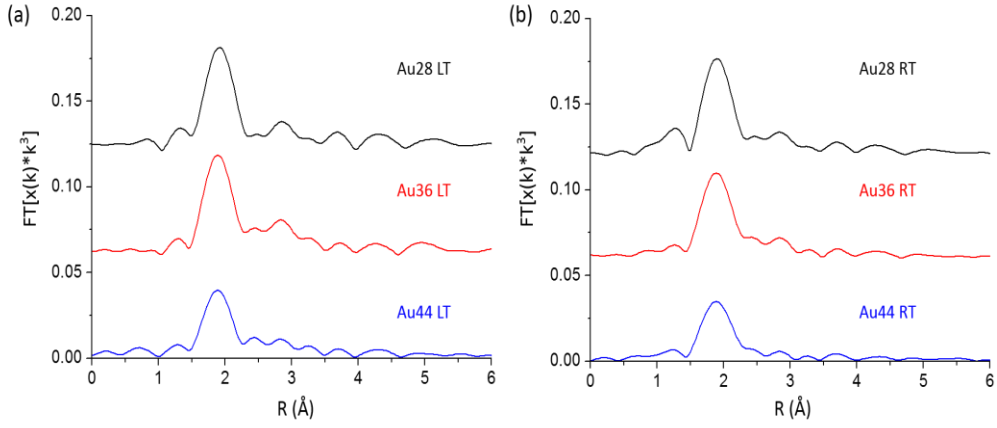


**Figure 3 - 2. FT-EXAFS of $Au_{28}$, $Au_{36}$ and $Au_{44}$ at RT and LT (In the comparison k-range of 3-11.25 $Å^{-1}$ was used for all the Au NCs).**

### 3.3.2 EXAFS analysis

In order to perform a reliable EXAFS analysis, the bond distance distribution of $Au_{44}$ was first studied based on the reported total structure.[66] Three scattering shells were found, which are displayed in Figure 3-3. The first shell with the shortest distance corresponds to the Au-S bonds in the NCs. The other two longer distance shells are caused by the Au-Au interactions. The shorter Au-Au shell ($Au-Au_1$) in the region of

2.707-2.849 Å accounts for the Au-Au bonding within the $Au_4$ unit of the NC core. The longer Au-Au shell (Au-$Au_2$) in the region of 2.877-3.104 Å corresponds to the long distance Au-Au interactions between surface, bridging and center Au atoms.

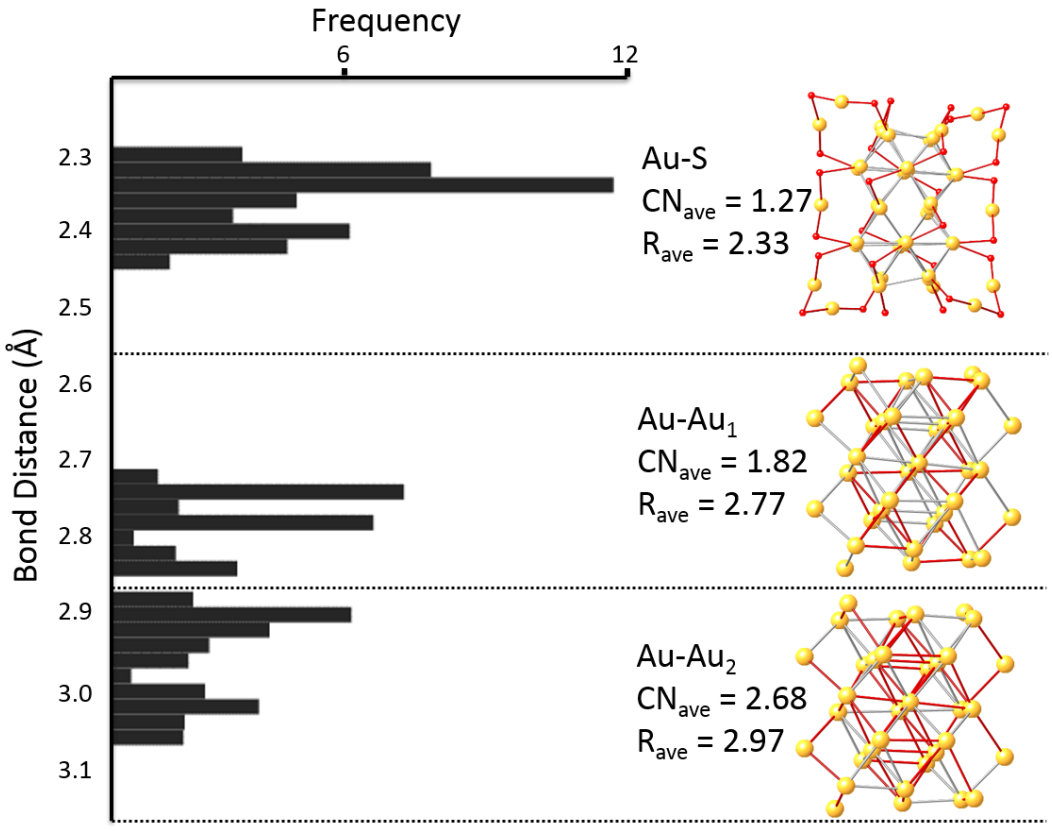


**Figure 3 - 3. Bond distance distribution for $Au_{44}$ and representative EXAFS scattering shells. The bonds in each shell are represented by red sticks.**

The bond distances from Au-S and Au-Au scattering shells in $Au_{44}$ were calculated by averaging all the bond distances within the same shell. The theoretical CN was calculated from the bond distance distribution (Figure 3-3). For the Au-S scattering shell, the average CN is found to be 1.27 ((56 Au-S bonds)/44 Au atoms). The average CN for Au-$Au_1$ and Au-$Au_2$ scattering shells are 1.82 ((40 Au-Au bonds) *2 / 44 Au

atoms) and 2.68 ((59 Au-Au bonds) *2 / 44 Au atoms), respectively. The calculated CN of the Au-S and two Au-Au scattering shells can then be used in the EXAFS fit, and were fixed in the EXAFS refinement process.

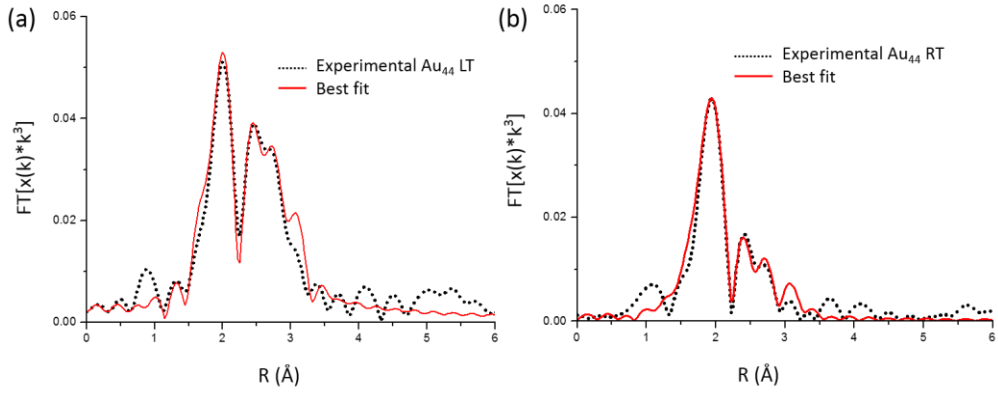


**Figure 3 - 4. Best fit for $Au_{44}$ spectra in (a) RT and (b) LT. (k-range: 3-14 $Å^{-1}$)**

To verify the reliability of the assignment of these three shells, a three-shell Au $L_3$-edge EXAFS (Au-S, Au-$Au_1$, Au-$Au_2$) fitting was performed for $Au_{44}$ at LT since the total structure was also obtained at LT.[66] Figure 3-4a. shows the best fit of $Au_{44}$ at 90 K and the fitting results are recorded in Table 3-1. From Table 3-1, it can be seen that the bond distances of Au-S (2.33 Å), Au-$Au_1$ (2.74 Å) and Au-$Au_2$ (2.93 Å) shell determined from the EXAFS refinement are very consistent with the calculated bond lengths from the total structure (i.e. Au-S: 2.33 Å, Au-$Au_1$: 2.77 Å, Au-$Au_2$: 2.97 Å). This verifies the reliability of the three-shell fitting method used in this work.

Next, we performed fits on the RT EXAFS to study the temperature-dependent properties of $Au_{44}$. The Au-S bond distance is essentially unchanged when the temperature is varied. However, the bond distances of both the Au-$Au_1$ and Au-$Au_2$

shells are found to be sensitive to the change in temperature. When the temperature increases from 90 K to 300 k, the bond distances of the Au-$Au_1$ shell display a negative thermal expansion (NTE) behavior, that is, a decrease from 2.744 Å to 2.724 Å (decrement = 0.020 Å). The Au-$Au_2$ shell also shows a NTE from 2.930 Å to 2.907 Å (decrement = 0.023 Å). It has been known that the tetrahedral $Au_4$ units within the gold core of other FCC-like clusters such as $Au_{28}$ and $Au_{36}$ play an important role in controlling their electronic properties. Therefore, we now focus on a close comparison of the temperature-dependent behavior of the Au-$Au_1$ shells for these three FCC-like clusters.

**Table 3 - 1. EXAFS fitting results from the multi-shell fitting procedure of $Au_{44}$ at both LT and RT. CN values are fixed to values from cluster models.**

| T (K) | Shells | CN[a] | R (Å) | $\sigma^2$ (Å$^2$) | $\Delta E_0$ (eV) |
|---|---|---|---|---|---|
| 90 (LT) | Au-S | 1.27 | 2.327 (9) | 0.0048 (6) | 1.60 (2) |
| | Au-$Au_1$ | 1.82 | 2.744 (9) | 0.0038 (4) | 1.60 (2) |
| | Au-$Au_2$ | 2.68 | 2.930 (12) | 0.008 (1) | 1.60 (2) |
| 300 (RT) | Au-S | 1.27 | 2.321 (10) | 0.0061 (6) | -0.10 (17) |
| | Au-$Au_1$ | 1.82 | 2.724 (17) | 0.0080 (9) | -0.10 (17) |
| | Au-$Au_2$ | 2.68 | 2.907 (24) | 0.012 (3) | -0.10 (17) |

**[a]CN were fixed according to the expected value determined from the total structure of $Au_{44}$ NCs**

In the previous studies, the Au-Au shell in $Au_{28}$ appears to be invariant to the temperature change, remaining at around 2.73(2) Å at both LT and RT.[82] Unlike $Au_{28}$, the Au-$Au_1$ shell in $Au_{36}$ displays a NTE, that is, the Au-Au distance decreases from 2.746(3) Å to 2.732(4) Å (decrement = 0.014 Å) as the temperature increases.[81] Comparing with $Au_{36}$, $Au_{44}$ shows an even more pronounced NTE in the Au-$Au_1$ shell. These results are summarized in Figure 3-5. Therefore, the change of bond distances in the Au-$Au_1$ shells shows an interesting size-dependent trend for the three Au NCs, that is, the NTE becomes stronger when the size of the Au NCs increases.

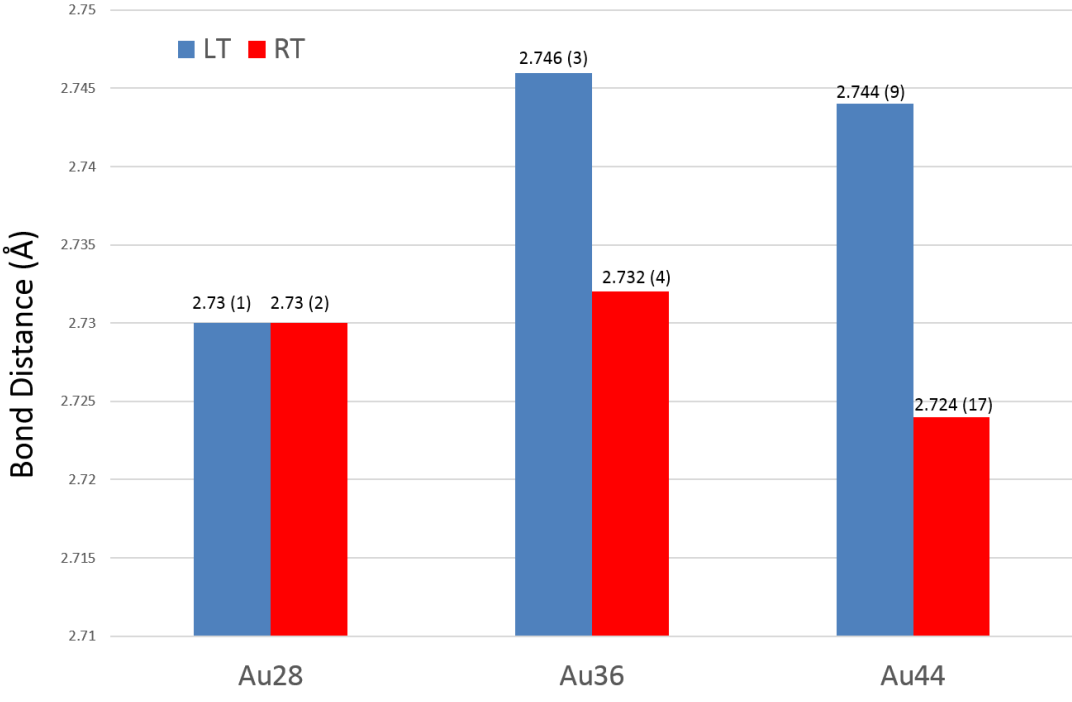


**Figure 3 - 5. Size-dependent NTE in $Au_{28}$, $Au_{36}$ and $Au_{44}$ NCs. (Bond distances of first Au-Au scattering shell in the three FCC-like Au NCs).**

To understand this phenomenon, their core structures, produced from X-ray crystallography data, are plotted in Figure 3-6 for a close comparison. As is shown in the figure, $Au_{28}$ has two sets of $Au_4$ units in the core, each set consisting of two $Au_4$ units connected by sharing one corner Au atom (Figure 3-6a). In the core of $Au_{36}$, two sets of $Au_4$ units were also observed. Each set consists of three $Au_4$ units connected by sharing two corner Au atoms (Figure 3-6b). The core of $Au_{44}$ also has two sets of $Au_4$ units, each set consisting of four $Au_4$ units which are connected by sharing three corner Au atoms. To more clearly see these $Au_4$ units within $Au_{44}$, the two sets of $Au_4$ units are plotted separately in Figure 3-6c).

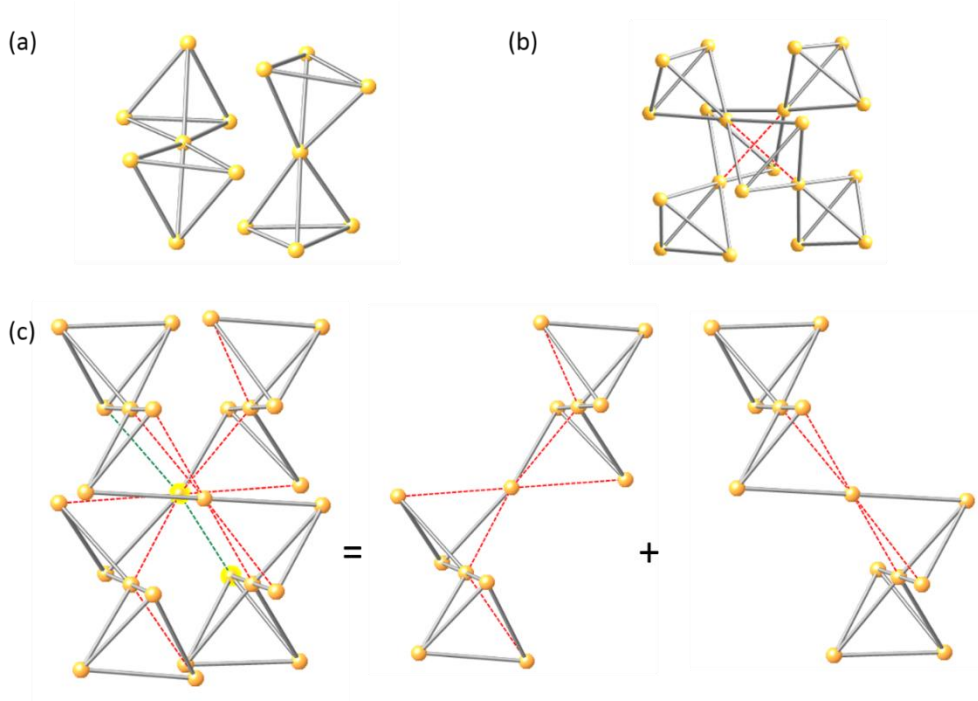


**Figure 3 - 6. The kernels (first Au-Au shell) of (a) $Au_{28}$, (b) $Au_{36}$ and (c) $Au_{44}$. (Red dash lines: missing Au-Au bonds. Green dash lines: extra Au-Au bonds.)**

Note that for all these models, the Au-Au bonds are identified based on a specific

bond distance (2.880 Å from bulk Au) which is the commonly used metallic Au-Au bond distance. When the Au-Au distances within the tetrahedral unit are longer than 2.880 Å, these Au-Au bonds are considered as non-metallic bonds (i.e. metallic bonds missing), and are shown with red dashed lines (Figure 3-6). In $Au_{28}$, all the metallic bonds are well maintained in the $Au_4$ units. As the size of the Au clusters increases, the $Au_4$ tetrahedrons begin to lose Au-Au metallic bonds. Specifically, two metallic bonds are missing in $Au_{36}$ and ten are missing in $Au_{44}$. (Figure 3-6a, b and c)

**Table 3 - 2. Number of Au-Au bonds in first Au-Au scattering shells (a), number of Au-Au bonds in the ideal first Au-Au scattering shells (b), and the ratio of a to b.**

| Au NCs | # of Au-$Au_1$ bonds (a) | Ideal # of Au-$Au_1$ bonds (b) | a/b (%) |
|---|---|---|---|
| $Au_{28}$ | 24 | 24 | 100 |
| $Au_{36}$ | 34 | 36 | 94 |
| $Au_{44}$ | 38 | 48 | 83 |

The missing metallic bonds shown in the Figure 3-6, indicate larger clusters have more defective $Au_4$ units within their core structures (“defective” or “defects”, borrowed from surface chemistry, is used to describe missing Au-Au bonds). Table 3-2 summarizes our quantitative analysis of the Au-Au metallic bonds for the $Au_4$ units in each cluster, including the ratio of observed metallic bonds to ideal metallic bonds

(for a perfect $Au_4$ tetrahedron) within the $Au_4$ units. As the size of the clusters increases, the ratio decreases from 100% for $Au_{28}$ to 94% for $Au_{36}$ and then to 83% for $Au_{44}$ (Table 3-2). In other words, when the cluster size increases, the Au core exhibits more pronounced defective $Au_4$ units.

Based on the information in Figure 3-6 and Table 3-2, we proceed to discuss the origin of the observed size-dependent NTE. For the smallest clusters, $Au_{28}$, the core structure has a perfect $Au_4$ based structure (i.e. no defect) and thus is the most rigid. Such a rigid core structure will exhibit the least amount of change in bond distance when temperature is varied. In contrast, the cores of larger clusters with a less perfect $Au_4$ bonding motif, will be less rigid, and thus, more sensitive to temperature change. As a result, larger clusters will exhibit more pronounced temperature-dependent NTE. In this comparative study, $Au_{44}$ was found to have the least rigid core structure, and thus, it exhibits the most pronounced NTE.

The size-dependent NTE trend we observed in FCC-like Au cores is an important finding which may help develop a better understanding of the growth mechanism of Au clusters. In these FCC-like Au clusters, the Au cores grow by the addition of $Au_4$ units to the two base sets which follow a "double helix" structure.[66] During the growth process, the bonding motif of $Au_4$ units within the core is not perfectly maintained and becomes more defective when the cluster size increases. This makes the Au core less rigid, and thus, more susceptible to change upon varied conditions (i.e. temperature).

## 3.4 Conclusions

In conclusion, the bonding properties of $Au_{44}$ was studied and compared with two other FCC-like Au clusters, $Au_{28}(SR)_{20}$ and $Au_{36}(SR)_{24}$. A multi-shell EXAFS fitting analysis was first established to reliably probe the site-specific bonding properties of the $Au_{44}$. Temperature-dependent EXAFS measurements indicate the existence of a negative thermal expansion behavior for the Au-Au interactions of the $Au_{44}(SR)_{28}$. Comparison of the bonding behavior of $Au_{44}(SR)_{28}$ with that of $Au_{28}(SR)_{20}$ and $Au_{36}(SR)_{24}$ shows an interesting size-dependent trend for the negative thermal expansion behavior of the first-shell Au-Au bonds. Specifically, the Au NCs with larger size exhibit more pronounced negative thermal expansion than the smaller ones. This observation can be understood as an effect related to the significant role of the bonding motif of $Au_4$ units within the Au cores. The bonding motif of the $Au_4$ units within the "double helix" structures of these clusters are observed to be less perfectly maintained when the size of FCC-like Au clusters increases. Our findings demonstrate the unique bonding properties of the FCC-like Au clusters, and may be further the understanding of the growth mechanism of these Au clusters.

# Chapter 4 – Hexagonal-Close-Packed (HCP)-like $Au_{30}(SR)_{18}$

*Manuscript in preparation* (*contributing authors:* Yang, R; Higaki, T; Ward, M; Jin, R.; Zhang, P.)

## Contributions

T.H. et al. synthesized $Au_{30}(SR)_{18}$ NCs. M.W. carried out the Au $L_3$-edge XAS measurements at the Sector20-BM beamline of the Advanced Photon Source (Argonne National Laboratory, IL, U.S.A.). R.Y. performed the data analysis, conducted *ab initio* calculations, and wrote the manuscript. P.Z. supervised R.Y. and helped with manuscript revision.

## 4.1 Introduction

The recently reported HCP-like $Au_{30}(SR)_{18}$ ($Au_{30}$ for short) has been attracting interest because of the special core geometry which has been found for the first time in NCs.[69,85,98,99] In this work, $Au_{30}(SR)_{18}$ is compared with icosahedral-like $Au_{25}(SR)_{18}$ ($Au_{25}$ for short) and face-centered cubic (FCC)-like $Au_{36}(SR)_{24}$ ($Au_{36}$ for short).

The total structures of $Au_{25}$, $Au_{30}$ and $Au_{36}$ are shown in Figure 4-1a, b and c, respectively.[74,76,85] To more clearly see the local structures, the staple site and Au cores are also displayed in Figure 4-1. Because of their similar surface environment, the comparison is carried out among these three NCs (Figure 4-1d, e and f: only S-Au-S-Au-S is found in surface areas). The eight dimeric $Au_2(SR)_3$ motifs in $Au_{36}$ are also considered as a mixture of bridging and staple motifs because of the different bonding

environment.

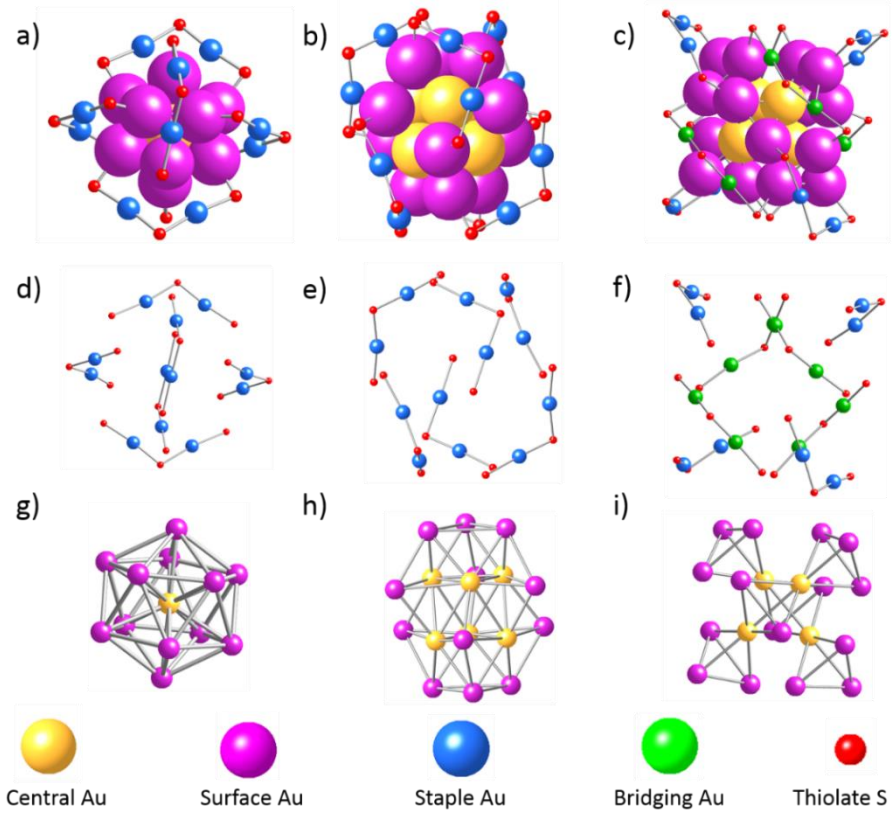


**Figure 4 - 1. Total structure of a) $Au_{25}$, b) $Au_{30}$, c) $Au_{36}$; staple-like and bridging motifs in d) $Au_{25}$, e) $Au_{30}$, f) $Au_{36}$ and core structures from g) $Au_{25}$, h) $Au_{30}$, i) $Au_{36}$ (yellow: central Au; purple: surface Au; blue: staple Au; green: bridging Au).**

Based on experimental data and theoretical simulations, the difference in electronic and bonding properties among $Au_{30}$, $Au_{25}$ and $Au_{36}$ NCs is systematically studied from their core, surface and staple sites. Temperature-dependent XAS measurements in association with multi-shell EXAFS fitting analysis is employed to study the thermal expansion behaviors.

## 4.2 Experimental Methods

### 4.2.1 Synthesis of $Au_{30}$

Details on the synthesis of $Au_{30}$ and total structure determination have been published by Tatsuya *et al*.[85] In the synthesis, 0.3 mmol of $HAuCl_4 \cdot 3H_2O$ was mixed with 0.348 mmol of TOAB and dissolved in 15 mL of methanol in a 50 mL round-bottom flask. After 15 min, the color of the stirred solution changed from yellow to reddish orange. 1.6 mmol of 1-adamantanetiol was then added at RT. The color was turned to yellowish-white. After 15 min, 3 mmol of $NaBH_4$ was added under vigorous stirring. The Au NCs were formed, and the solution appears black in color. After stirring for 1 week, the black sticky precipitate was collected from solution. The clusters were then washed with dichloromethane and extracted from the residue with benzene. Approximately 20% of yield was finally achieved.

### 4.2.2 X-ray absorption spectroscopy (XAS)

Au $L_3$-edge XAS measurements were carried out in transmission mode at the Sector20-BM beamline of the Advanced Photon Source (Argonne National Laboratory, IL, U.S.A.). $Au_{30}$ powder samples were packed into Kapton film pouches, sealed and folded to ensure adequate X-ray absorption. A Au foil reference was measured simultaneously for calibration of the energy of Au $L_3$ absorption edge. XAS data was collected at both LT using a helium-cooled cryostat chamber and RT under ambient

conditions. Furthermore, the details of XAS measurements of $Au_{25}$ and $Au_{36}$ have been published elsewhere.[81,95]

### 4.2.3 Data analysis

The simulated first derivative of XANES spectra in the three NCs were generated by using FEFF8.2 computer code.[86] In the comparison between experimental first derivative XANES and site-specific simulations, the simulated first derivative XANES of $Au_{25}$, $Au_{30}$ and $Au_{36}$ was generated from the Au atoms in different surface, staple and core sites based on the published total structures.[74,76,85] One Au site contains the selected Au atom and its connected Au or S atoms. The types of Au sites are dependent on their bonding environment. In the analysis, only one Au atom in each type of Au site was selected and used in the simulation. Moreover, two surface and staple sites were found in $Au_{30}$, two types of staple sites and two types of bridging sites are found in $Au_{36}$. The other Au sites in the three NCs show a single type of bonding environment. Furthermore, the y-axis of simulated first derivative XANES was normalized by multiplying weight percentage (*i.e.*, number of Au atoms in each site / total number of Au atoms).

The XAS data processing and fitting were performed using the WinXAS 3.1 software package[94] and FEFF8.2 computer code.[86] In the refinement process, the amplitude reduction factor ($S_0^2$) of 0.9 was obtained by fitting the Au foil EXAFS and fixed for the EXAFS fitting of Au clusters. For multi-shell EXAFS fitting, CN of Au-

S and Au-Au shells were fixed based on the published $Au_{30}$ total structure. A k-range of 3-10.7 $Å^{-1}$ was used for fitting the EXAFS of $Au_{30}$ and a longer k-range (3.2-12 $Å^{-1}$) was used for qualitatively comparing the EXAFS of $Au_{30}$, $Au_{25}$ and $Au_{36}$ in order to make their k-range consistent for the comparison. $E_0$ shift values from first (Au-$Au_1$) and second Au-Au shells (Au-$Au_2$) were correlated to reduce the number of free running parameters, allowing for the incorporation of these two scattering shells.

## 4.3 Results and Discussion

### 4.3.1 Experimental and theoretical XANES

The Au $L_3$-edge XANES of $Au_{25}$, $Au_{30}$ and $Au_{36}$ is first compared in Figure 4-2a. The obvious difference in near edge feature is observed among the three NCs. For clarity, the XANES ranged from 0 eV to 14 eV is shown in the inset of Figure 4-2a. (right bottom in Figure 4-2a). To more clearly see these features, the technique of first derivative XANES of the three NC samples is exhibited in Figure 4-2b. As shown in the figure, all the three NCs have similar feature in lower energy region and are labeled as feature A. The only feature around 13 eV from $Au_{30}$ is labeled as feature B. In order to understand the origin of these XANES features for each Au NCs, experimental first derivative XANES is further studied by comparing with their site-specific simulations.

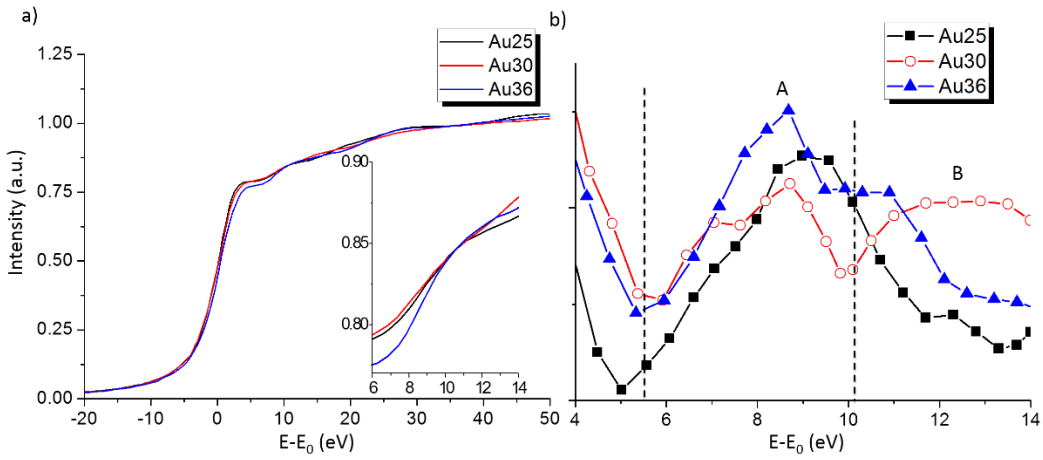


**Figure 4 - 2. Experimental Au $L_3$-edge a) XANES and, b) their first derivative of $Au_{25}$, $Au_{30}$ and $Au_{36}$.**

To perform a reliable comparison between experimental and simulated first derivative XANES, the well-studied $Au_{25}$ from our previous work is first studied. In Figure 4-3, the experimental data of $Au_{25}$ is displayed together with the site-specific simulations from surface, staple and core sites. Feature A from experimental data exhibits a match with those from simulated surface and staple sites. Therefore, these results prove that the simulation method is reliable. When the simulated first derivative XANES is calculated by the weight percentage, the simulation from core site has almost no contribution due to the negligible amount of Au atoms.

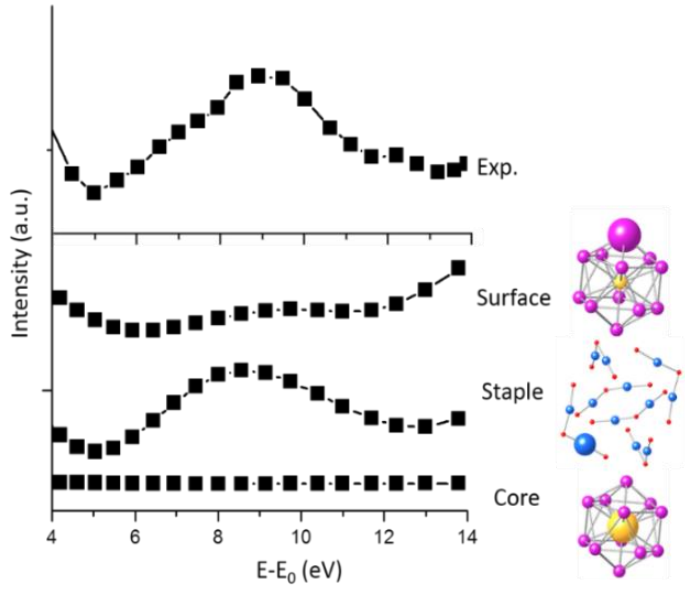


**Figure 4 - 3. Experimental first derivative XANES of $Au_{25}$ is shown on the top. The simulated first derivative XANES is generated from surface, staple and core sites and exhibited respectively.**

Next, the experimental first derivative XANES from all the three NCs in association with their site-specific simulations are shown in Figure 4-4. It is found that feature A from experimental first derivative XANES in all the three NC samples is contributed by both surface and staple sites. Feature B from $Au_{30}$, which is very unique from the other two, is significantly influenced by its surface site. Specifically, the simulated XANES from surface site in $Au_{30}$ shows a blue-shifted feature in lower energy region by comparing with those from $Au_{25}$ and $Au_{36}$ ("blue-shifted" and "red-shifted" is used to describe the feature which is shifted at higher and lower energy, respectively). This blue-shifted feature in the simulation is consistent with feature B in experimental data from $Au_{30}$. Therefore, features A and B in experimental data from

$Au_{30}$ should correspond to the overlap of simulated XANES from its surface and staple sites. The difference in staple site simulations of the three NCs is much less significant. The results from Figure 4-4 indicate that the difference in experimental XANES is mainly influenced by the surface sites. Note that there is ~1eV mismatch between feature A of $Au_{30}$ experimental data and the simulation of its staple site. However, this mismatch should not influence the double-peak shape of the overall simulated XANES.

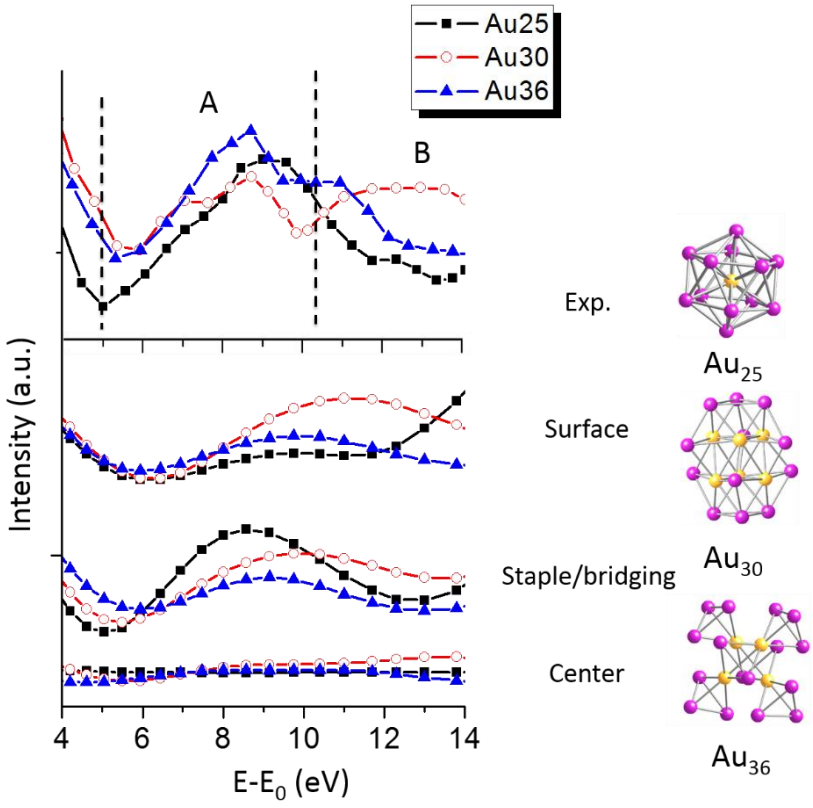


**Figure 4 - 4. Comparison of experimental first derivative XANES with simulated first derivative of XANES from surface, staple and core sites between $Au_{25}$, $Au_{30}$ and $Au_{36}$. Core structural models with specific staple sites of $Au_{25}$, $Au_{30}$ and $Au_{36}$ are shown on the right hand (yellow: central Au; purple: surface Au). Note that the higher energy feature in the simulations are not completely shown as the EXAFS signal starts to appear in the higher energy region.**

To understand how the difference in surface sites influence the XANES, the bond distance distributions of representative surface sites are plotted in Figure 4-5a, b and c. The corresponding structural models of surface sites are also presented. It is clear to see that surface site from $Au_{25}$ has the longest averaged Au-Au bond distance and the surface site from $Au_{30}$ has the shortest averaged Au-Au bond distance. In order to understand the relationship between the difference in Au-Au bond distance and XANES, a test of lattice expansion effect is performed. In this test, the simulated XANES from surface sites is compared with simulations using expanded Au-Au bond distance, that is, all the bond distances are increased by 10%. In Figure 4-5d, e and f, the simulations for all the three NCs exhibit a red-shift when the Au-Au bond distance increases. Based on the results from this test, the difference among simulated XANES from surface sites can be explained. The blue-shifted surface-site simulations from $Au_{30}$ is caused by the shorter Au-Au bond distance.

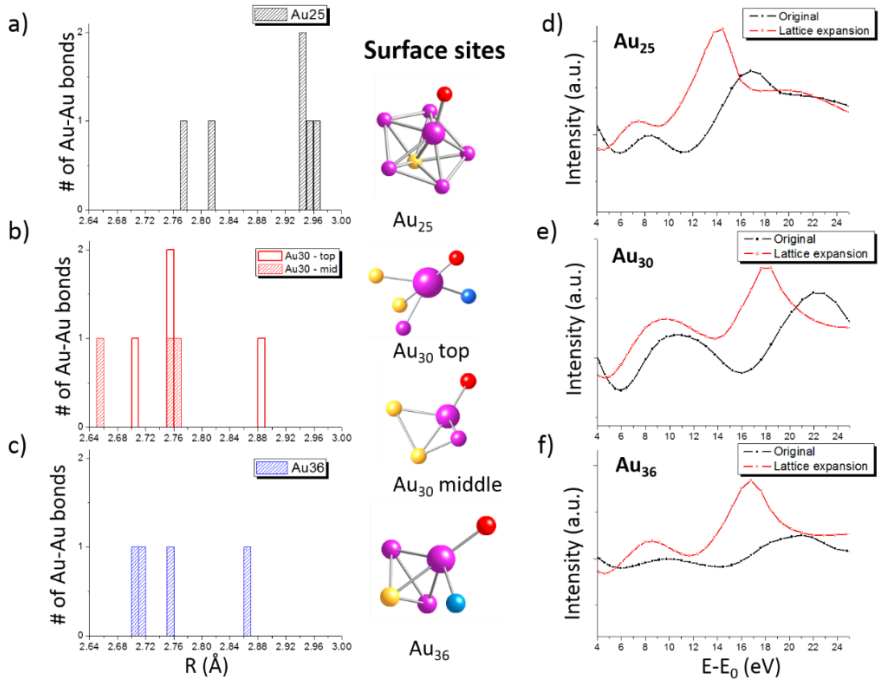


**Figure 4 - 5. Bond distance distribution of surface sites in a) $Au_{25}$, b) $Au_{30}$ and c) $Au_{36}$ are shown. The corresponding surface sites are exhibited on the right (the selected surface Au atoms for simulations are enlarged; yellow: central Au; purple: surface Au; blue: staple Au; red: S). The simulated bond distance tests of d) $Au_{25}$, e) $Au_{30}$ and f) $Au_{36}$ are also exhibited. Based on the surface site bonding environment, there are two types of surface sites in $Au_{30}$ (six Au atoms in top and bottom areas and six Au atoms in middle area), but only one type of surface Au site in $Au_{25}$ and $Au_{36}$.**

### 4.3.2 Temperature-dependent EXAFS

The FT-EXAFS of $Au_{25}$, $Au_{30}$ and $Au_{36}$, collected at RT, are plotted in Figure 4-6. The most intense peaks overlapped around 2 Å represents Au-S scattering. The peaks caused by Au-Au scatterings within first (Au-$Au_1$) and second Au-Au shells (Au-$Au_2$) appears around 2.7 Å and 2.9 Å, respectively. These features from Au-S and Au-Au

scattering allow us to confirm that the three-shell Au $L_3$-edge EXAFS among the three NCs are comparable. More detailed structural information of these scattering shells in $Au_{30}$ was obtained by the refinement of FT-EXAFS.

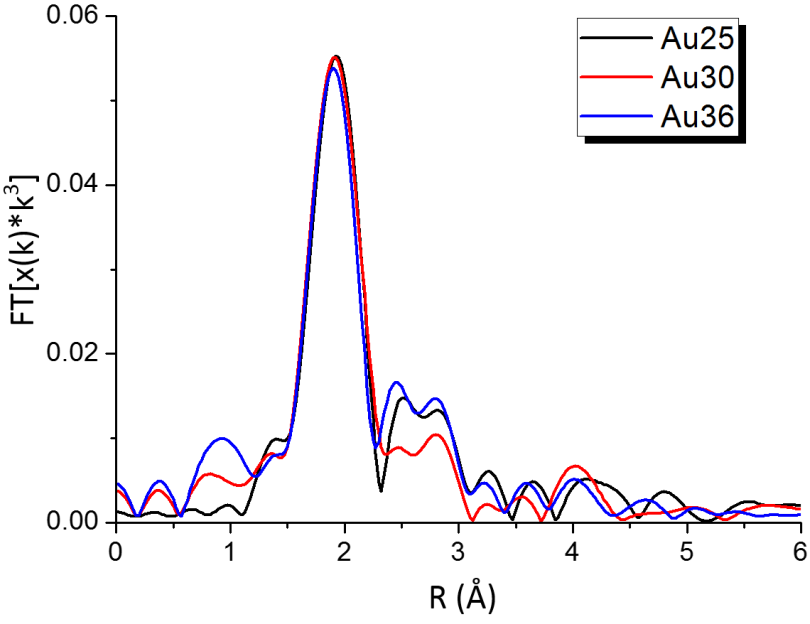


**Figure 4 - 6. Experimental FT-EXAFS of $Au_{25}$, $Au_{30}$ and $Au_{36}$.**

To perform a reliable EXAFS analysis, the bond distance distribution of $Au_{30}$ was studied based on the reported total structure.[85] The first three scattering shells are displayed in Figure 4-7. The first shell with shortest bond distances is caused by Au-S scattering (red bars). As shown in Figure 4-7, in $Au_{30}$, the first shell Au-Au interaction, Au-$Au_1$ (2.656 Å to 2.764 Å), accounts for the Au-Au bonding within the core ($Au_{surface}$-$Au_{core}$). The second shell Au-Au interaction, Au-$Au_2$ (2.884 Å to 2.942 Å), corresponds to the interaction in a longer distance between surface, staple and core Au atoms ($Au_{core}$-$Au_{core}$, $Au_{surface}$-$Au_{staple}$).

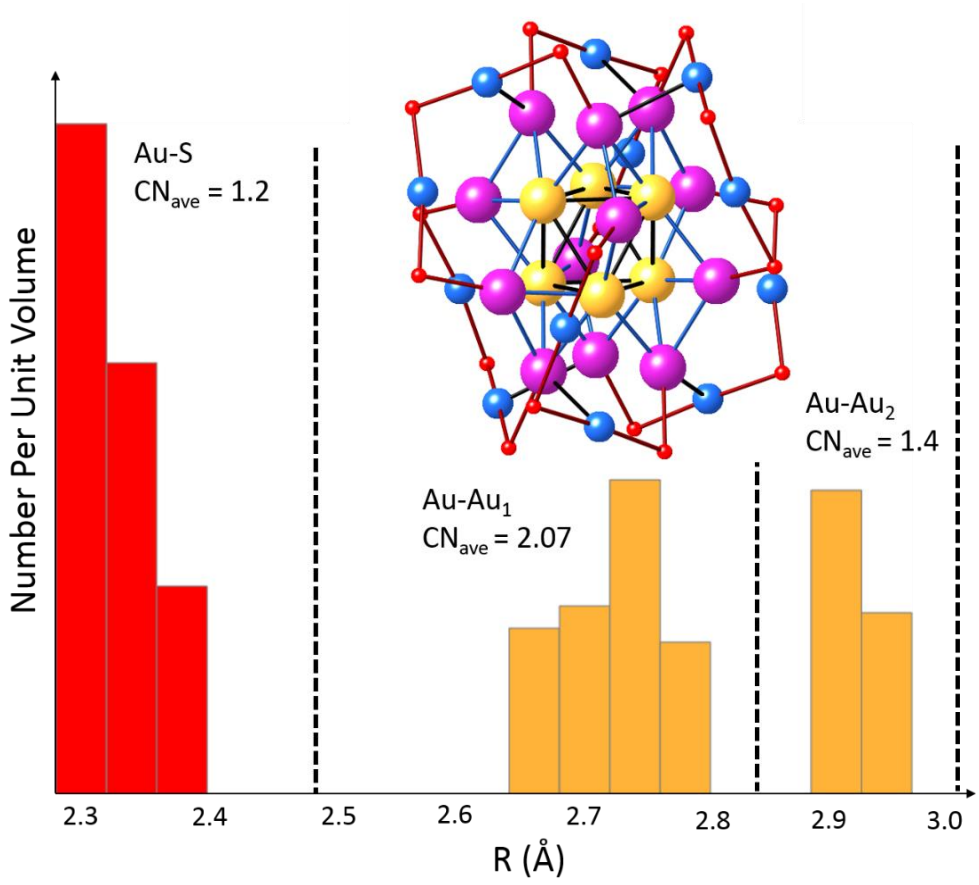


**Figure 4 - 7. Bond distribution for $Au_{30}$ and representative EXAFS scattering shells. Au-S, Au-$Au_1$, Au-$Au_2$ interactions are represented by red, blue and black sticks respectively.**

The theoretical CN was calculated based on the bond distance distribution. The averaged CN for Au-S, Au-$Au_1$, Au-$Au_2$ scattering shells are 1.20 ((36 Au-S bonds) / 30 Au atoms), 2.07 ((21 Au-Au bonds) * 2 / 30 Au atoms) and 1.40 ((31 Au-Au bonds) * 2 / 30 Au atoms), respectively. The theoretical CNs of the three shells are then used as the fixed CN values in the EXAFS refinement process.

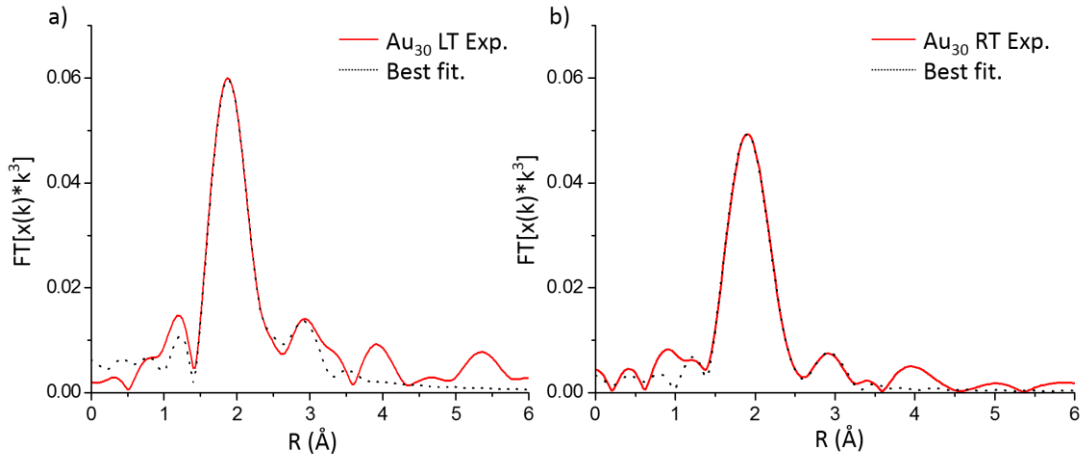


**Figure 4 - 8. Experimental FT-EXAFS (k-range: 3.2-10.7 Å) and best fit for $Au_{30}$ at (a) LT and (b) RT.**

To study the temperature-dependent properties of $Au_{30}$, a three-shell Au $L_3$-edge EXAFS (Au-S, Au-$Au_1$, Au-$Au_2$) was performed at 90 K (LT) and 298 K (RT). Figure 4-8a and b shows the best fits and their fitting results are recorded in Table 4-1. The Au-S bond distance show negligible change (decrement = 0.006 Å) when the temperature is varied. However, the bond distance of Au-$Au_1$ and Au-$Au_2$ are sensitive to the change of temperature. When the temperature increases from 90 K to 298 K, the bond distance of Au-$Au_1$ decreases from 2.77 Å to 2.69 Å (decrement = 0.08 Å). The Au-$Au_2$ also shows a decrement from 3.00 Å to 2.85 Å (decrement = 0.15 Å). This phenomenon in Au-$Au_1$ and Au-$Au_2$ shells is called negative thermal expansion (NTE) which has been found in FCC-like Au NCs such as $Au_{36}$ and $Au_{44}$.[81,83]

**Table 4 - 1. EXAFS multi-shell fitting results of $Au_{30}$ at both LT and RT.**

| T (K) | Shells | CN | R (Å) | $\sigma^2$ (Å$^2$) | $\Delta E_0$ (eV) |
|---|---|---|---|---|---|
| **90 (LT)** | Au-S | 1.20 | 2.32 (1) | 0.0006 (4) | -1 (2) |
| | Au-$Au_1$ | 2.07 | 2.77 (3) | 0.006 (2) | 6 (5) |
| | Au-$Au_2$ | 1.40 | 3.00 (6) | 0.012 (9) | 6 (5) |
| **298 (RT)** | Au-S | 1.2 | 2.311 (4) | 0.0029 (2) | -2 (1) |
| | Au-$Au_1$ | 2.07 | 2.69 (2) | 0.008 (2) | 1 (2) |
| | Au-$Au_2$ | 1.40 | 2.85 (3) | 0.009 (3) | 1 (2) |

**[a] CN values are fixed to the values calculated from total structure (No errors for fixed CN values).**

The core geometry effect on the thermal bonding behaviors among the three NCs was then examined. Here, the comparison of the temperature-dependent bonding behavior for Au-$Au_1$ was inspected for $Au_{25}$, $Au_{30}$ and $Au_{36}$, and is plotted in Figure 4-9. The data of $Au_{25}$ and $Au_{36}$ are used from previous publication.[81,95] As shown in Figure 4-9, the $Au_{25}$ shows a positive thermal expansion, with an increase from 2.80 Å to 2.82 Å, when temperature increases.[95] In contrast, both $Au_{30}$ and $Au_{36}$ shows NTE behavior. In $Au_{36}$, the bond distance decreases from 2.746(3) Å to 2.732(4) Å as the temperature increases.[81] By comparing with $Au_{36}$, the bond distance of Au-$Au_1$ in $Au_{30}$ displays a much more significant NTE (decrement = 0.078 Å) (Figure 4-9).

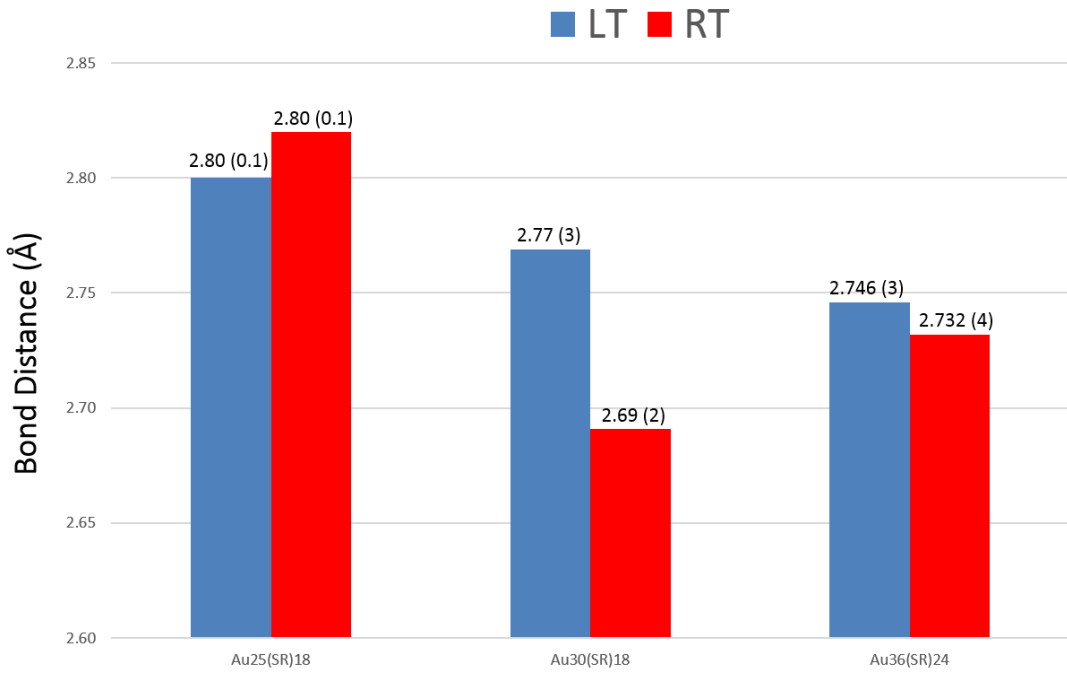


**Figure 4 - 9. Bond distances of Au-Au$_1$ in Au$_{25}$, Au$_{30}$ and Au$_{36}$ NCs at LT (blue) and RT (red).**

To gain a better understanding of this core expansion/contraction phenomenon, the core structures of $Au_{25}$, $Au_{30}$ and $Au_{36}$ NCs are displayed in Figure 4-10. The smallest structural unit in the core of $Au_{25}$ is the icosahedral $Au_{13}$ and the smallest Au units in $Au_{30}$ and $Au_{36}$ are tetrahedral $Au_4$. As a result, the core of $Au_{25}$ should be more metal-like then those of the other two NCs. In other words, $Au_{25}$ has higher metallicity. the more metal-like $Au_{13}$-unit in $Au_{25}$ is much more metal-like which leads shows a positive thermal expansion which is commonly observed in bulk metals. In contrast, $Au_4$ units in $Au_{30}$ and $Au_{36}$ are more molecular-like and exhibit NTE.

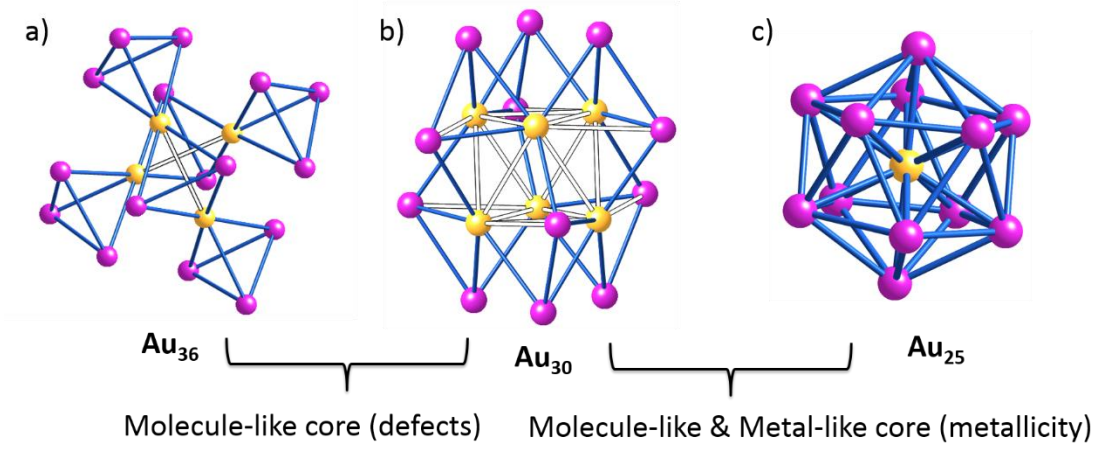


**Figure 4 - 10. Molecule-like core structure with defects in a) $Au_{30}$ and b) $Au_{36}$ are exhibit using Au-Au bonds with different colors (blue: surface bonds; white: miss metallic Au-Au bonds). The metal-like core structure from c) $Au_{25}$ are shown on the right. (Figure 4-10c: defects are not shown; all Au-Au bonds are colored in blue)**

To understand the different NTE behaviors between $Au_{30}$ and $Au_{36}$, we closely compare the core Au-Au bonding within these two NCs in Figure 4-10. The Au cores in $Au_{30}$ and $Au_{36}$ which consist of $Au_4$-units, exhibits more molecule-like structure (or lower metallicity). The defective Au core in FCC-like NCs was found to play an important role in the temperature-dependent bonding properties which leads to the NTE. Here, the defects mean the missing of metallic Au-Au bonds (2.880 Å) in the gold cores. In Figure 4-10a and b, $Au_{36}$ and $Au_{30}$ have very different number of defects, that is two and 18 missing (white sticks in Figure 4-10) Au-Au metallic bonds in each NC core. The more defective core in $Au_{30}$ results in a less rigid core which is more easily changed in varied environmental conditions. As a result, the less perfectly maintained core of $Au_{30}$ shows a more pronounced NTE when temperature changes.

These results are also consistent with the trend of NTE bonding behaviors in the series of FCC-like Au NCs where the level of core defect is systematically changed.[83] Based on these results, the defects and metallicity of gold cores are very important in determining their temperature-dependent bonding behavior.

## 4.4 Conclusion

In summary, XAS measurements in association with theoretical calculations probed the unique bonding properties of $Au_{30}(SR)_{18}$ with comparisons to icosahedral-like and FCC-like Au NCs with similar surface bonding environments. It was found that the early XANES region of thiolate-stabilized Au NCs is significantly influenced by the gold-gold bonding environment in surface sites. This finding is useful toward better understanding the temperature-dependent structural properties among HCP-like Au NCs. In particular, our results based on temperature-dependent EXAFS indicate the NTE in molecule-like $Au_{30}(SR)_{18}$ and $Au_{36}$ is strongly determined by the defects in the core, and positive thermal expansion in metal-like $Au_{25}$ is caused by the special metallicity with more rigid character. The more pronounced NTE in $Au_{30}(SR)_{18}$ is strongly dependent on its unique bonding properties due to a more defective core. This work suggests that HCP-like $Au_{30}(SR)_{18}$ with unique bonding properties should be treated differently from the other thiolate stabilized gold nanoclusters, and may be further provides the methods for studying other HCP-like gold nanoclusters in the

future.

# Chapter 5 – Body-Centered Cubic (BCC)-like $Au_{38}S_2(SR)_{20}$

*Manuscript in preparation* (*contributing authors:* Yang, R; Liu, C.; Ward, M.; Jin, R.; Zhang, P.)

## Contributions

C.L. et al. synthesized the $Au_{38}S_2(SR)_{20}$ nanoclusters. M.W. carried out the Au $L_3$-edge XAS measurements at the Sector20-BM beamline of the Advanced Photon Source (Argonne National Laboratory, IL, U.S.A.). R.Y. performed the data analysis, conducted *ab initio* calculations, and wrote the manuscript. P.Z. supervised R.Y. and helped with manuscript revision.

## 5.1 Introduction

Recently, the first BCC-like Au NC, composed of 38 Au atoms protected by 20 thiolate ligands and two sulfide atoms ($Au_{38}S_2(SR)_{20}$, R = $C_{10}H_{15}$), was reported.[84] This BCC-like $Au_{38}$ (BCC-$Au_{38}$ for short) is interesting because of the special core geometry that has never been found previously.[84] Bi-icosahedral like $Au_{38}(SR)_{24}$ (biico-$Au_{38}$ for short) is used as a comparison due to the similar component and cluster size.[96]

As shown in Figure 5-1, BCC-$Au_{38}$ consists of $Au_{30}$ core and 4 $Au_2(SR)_3$ staple like motifs (Figure 5-1a and b). The BCC-like Au core is further found to have 6 central Au atoms protected by 6 $Au_4$ units (Figure 5-1c) and 6 sulfide Au atoms (Figure 5-1d:

Au atoms that connects to sulfide S) on the top.[84] In comparison, biico-$Au_{38}$ consists of $Au_{23}$ core, 3 $AuS_2$ and 6 $Au_2(SR)_3$ staple like motifs (Figure 5-1e and f). In this bi-icosahedral like Au core, 5 central Au atoms are protected by 18 surface Au atoms (Figure 5-1g).[96] Importantly, no sulfide Au atoms are found in this NC.

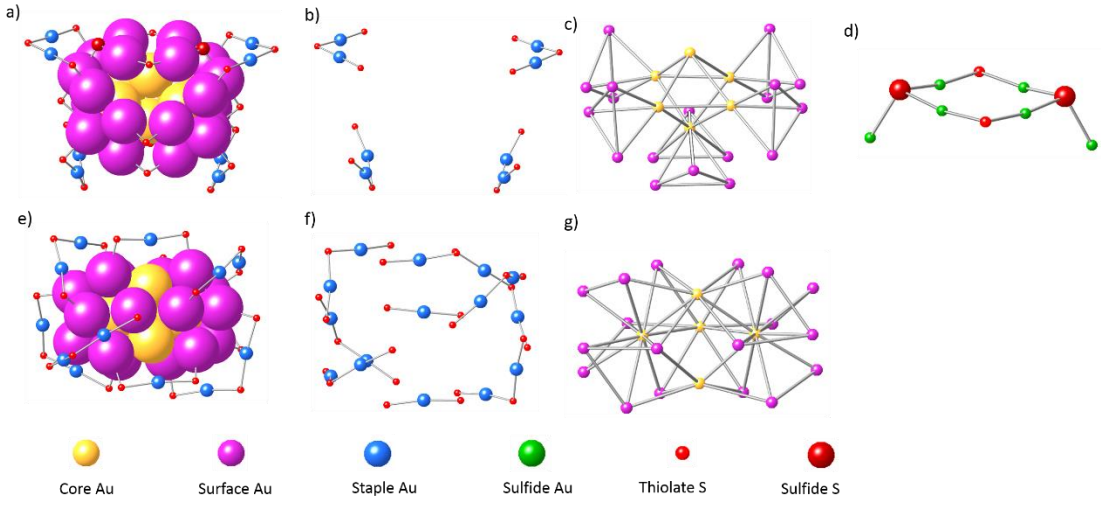


**Figure 5 - 1. a) Total structure, b) staple-like motifs, c) Au core and d) sulfide Au atoms of BCC-$Au_{38}$; e) total structure, f) staple-like motifs, g) Au core of biico-$Au_{38}$. (yellow: central Au; purple: surface Au; blue: staple Au; red: sulfur atoms (-SR); enlarged red balls in model: sulfide atoms (-S)).**

To study the bonding properties in BCC-$Au_{38}$, X-ray absorption spectroscopy (XAS) experiments were performed. Utilizing XANES, together with theoretical calculations, the electronic and bonding properties of BCC-$Au_{38}$ were studied from surface, staple and core sites. Furthermore, EXAFS analysis helped to understand the expansion behavior of Au-Au bonding upon solvation.

## 5.2 Experimental Methods

### 5.2.1 Synthesis of BCC-$Au_{38}$ and biico-$Au_{38}$

The BCC-$Au_{38}$ NCs were synthesized using a size-focusing method.[84] First, 0.2 mmol of $HAuCl_4 \cdot 3H_2O$ was mixed with 0.2 mmol of tetraoctylammonium bromide (TOAB) in 15 ml THF at RT, and stirred for 30 mins. 0.8 mmol adamantanethiol was then added into the solution. After stirring, the solution became colorless. After that, $NaBH_4$ solution was added at once. The solution became dark immediately. After 10 mins, the black product was dried and washed with methanol for four times. Then, $CH_2Cl_2$ was added to extract the solid. The insoluble species were discarded. After extracting twice, the solution was evaporated to dryness, and 50 mg solid (NCs) was obtained. In size focusing step, the produced NCs containing a mixture of difference sizes were mixed with excess adamantanethiol and dissolved in 2 ml toluene. The solution was heated to 90 °C for 24 h. The final product was washed with methanol for 4 times and extracted using $CH_2Cl_2$. Finally, the crystallization was carried out with vapor diffusion methods.

For biico-$Au_{38}$ synthesized by Huifeng et al., a similar synthesis method was employed.[96] Briefly, 0.5 mmol of $HAuCl_4 \cdot 3H_2O$ was mixed with 2.0 mmol of glutathione (GSH) in 20 mL of acetone at RT under vigorous stirring. After 20 mins, the yellowish product was cooled to ~ 0 °C. When the 5 mmol of $NaBH_4$ solution was added and stirred for ~ 20 mins, black Au NCs were obtained. The mixture was

then mixed with 0.3 mL of ethanol, 2 mL of toluene and 2 mL of $PhCH_2CH_2SH$. The solution was heated to 80 °C for 40 h. After washing with ethanol and crystallization, the biico-$Au_{38}$ NCs was produced. Both the syntheses produced Au NCs in high purity which is supported by mass spectrometer data.

### 5.2.2 X-ray absorption spectroscopy (XAS)

The Au $L_3$-edge XAS measurements were carried out in transmission mode at the Sector20-BM beamline of the Advanced Photon Source (Argonne National Laboratory, IL, U.S.A.). $Au_{38}S_2(SR)_{20}$ powder samples were packed into Kapton film pouches, sealed and folded to ensure high quality EXAFS signals were collected. Both solid and liquid $Au_{38}S_2(SR)_{20}$ samples were measured at RT. Furthermore, the details of XAS measurements of biico-$Au_{38}$ have been published elsewhere.[96]

### 5.2.3 Data analysis

The XAS data processing and fitting were performed using the WinXAS 3.1 software package[94] and FEFF8.2 computer code.[86] In the refinement process, the amplitude reduction factor ($S_0^2$) of 0.9 was obtained by fitting the Au foil EXAFS and fixed for the EXAFS fitting of Au clusters. For multishell EXAFS fitting, CN of Au-S and Au-Au shells were fixed based on the published BCC-$Au_{38}$ total structure. A k-range of 3.0 - 12.3 $Å^{-1}$ was used for fitting the EXAFS of BCC-$Au_{38}$ and a shorter k-range (3.4 - 12.1 $Å^{-1}$) was used for qualitatively comparing the EXAFS of the two

clusters in order to make their k-range consistent for the comparison. All the $E_0$ shift values were correlated to reduce the number of free running parameters, allowing for the incorporation of three scattering shells.

In theoretical calculations, only one Au atom in each type of Au site is selected and used in the simulation. Furthermore, Y-axis of simulated first derivative XANES is normalized by multiplying weight percentage (ie. number of Au atoms in each site / total number of Au atoms).

## 5.3 Results and Discussion

### 5.3.1 Experimental and theoretical XANES

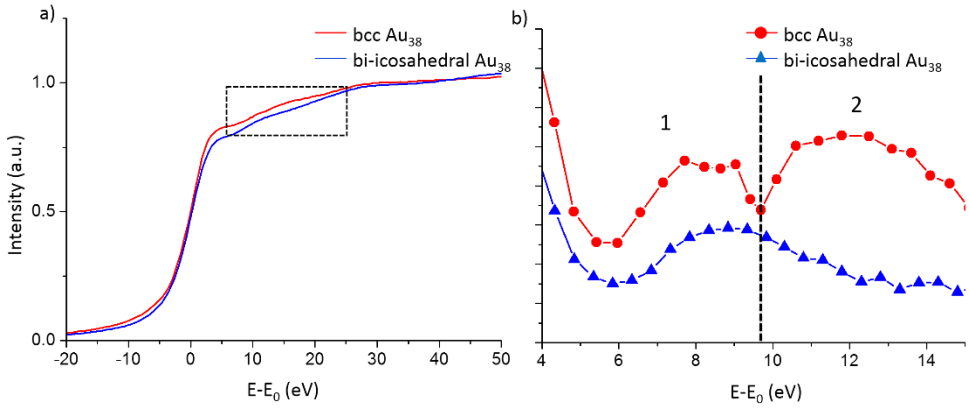


**Figure 5 - 2. Au $L_3$-edge a) XANES and, b) their first derivative of BCC-$Au_{38}$ and biico-$Au_{38}$.**

Au $L_3$-edge XANES of BCC-$Au_{38}$ and biico-$Au_{38}$ is first compared in Figure 5-2a. The near-edge of XANES attracts our interest due to the importance in determining

NC electronic properties. The near-edge region XANES with distinctive features between the two NCs is selected in Figure 5-2a. To more clearly see the difference, the features in the selected region are transferred to first derivative and shown in Figure 5-2b. Inspecting the first derivative XANES, BCC-$Au_{38}$ has two broad bands at 8 eV and 12 eV, respectively. In contrast, biico-$Au_{38}$ exhibits only one broad band around 9 eV. To study the difference between these two NCs, the experimental data is compared with their site-specific simulations (in a selected energy region: 4 eV ~ 14 eV) which is calculated by FEFF8.2 computer code.[86]

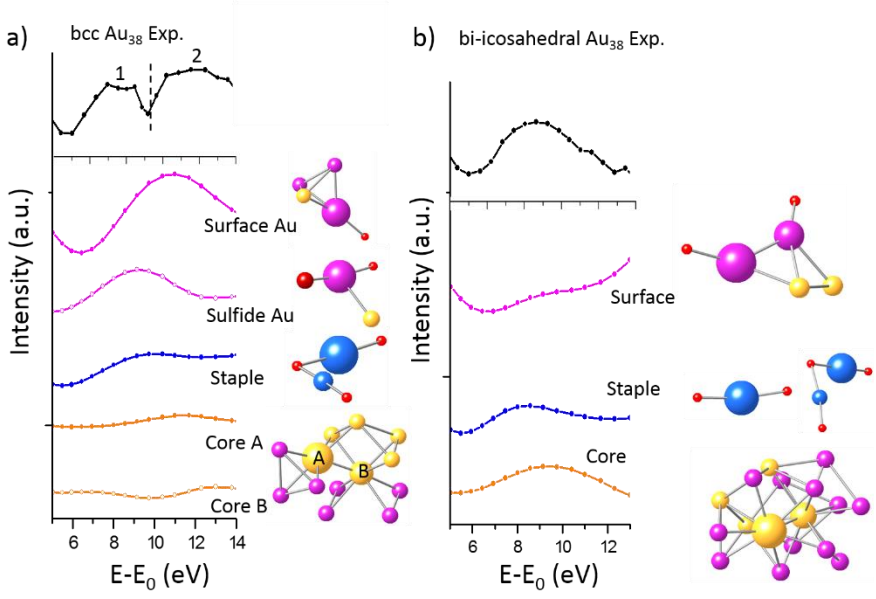


**Figure 5 - 3. Comparison of experimental first derivative XANES with simulated first derivative of XANES from surface, staple and core sites for both a) BCC-$Au_{38}$ and b) biico-$Au_{38}$. The corresponding surface, staple and core sites are exhibited on the right (the selected Au atoms in each site are enlarged).**

In Figure 5-3a, experimental data of BCC-$Au_{38}$ and the simulations from surface, staple and core sites are compared. For clarity, the two features in experimental

XANES from BCC-$Au_{38}$ are labeled as feature 1 and feature 2. It was found that the sulfide Au and staple sites help to form the experimental feature 1 and 2. Feature 2 in experimental data is only caused by the blue-shifted feature from surface Au site . The experimental XANES from biico-$Au_{38}$ is shown in Figure 5-3b. The corresponding site-specific simulations from surface, staple and core sites are also shown below. As shown in the figure, all the simulations have a single feature which corresponds to the experimental data. Therefore, the experimental XANES, contributed by surface, staple and core sites, shows only one intense peak.

Based on these results, surface Au site in BCC-$Au_{38}$ plays an important role in determining the difference in the XANES of the two NCs. Surface site refers to the surface Au atom within the $Au_4$ units. To have a better understanding of the difference in surface sites from BCC-$Au_{38}$, the bond distance distribution of surface and sulfide sites are plotted in Figure 5-4 a and b, respectively. In comparison, Au-Au bond distances from surface Au site are significantly shorter than those from sulfide Au site. This implies the bond distance might affect the first derivative XANES. Therefore, a bond distance test is performed on the simulated XANES from the surface and sulfide sites. In the test, the first derivative XANES of the surface and sulfide sites is simulated using 10% expanded Au-Au bond distances. As shown in Figure 5-4 c and d, the first derivative XANES from the test shifts to lower energy when the Au-Au bond distance increases. The bond distance effect is then used to understand the blue-shifted feature in surface Au site. Based on the results from bond distance test, the shorter Au-Au bond

distances from surface Au leads to the blue-shifted feature observed in the experimental first derivative. The Au-Au bond distance in $Au_4$ units, which form the surface site, is then highlighted due to the importance in influencing near-edge XANES. This finding further shifts our attention to study their corresponding local structures. More detailed discussion will next be presented.

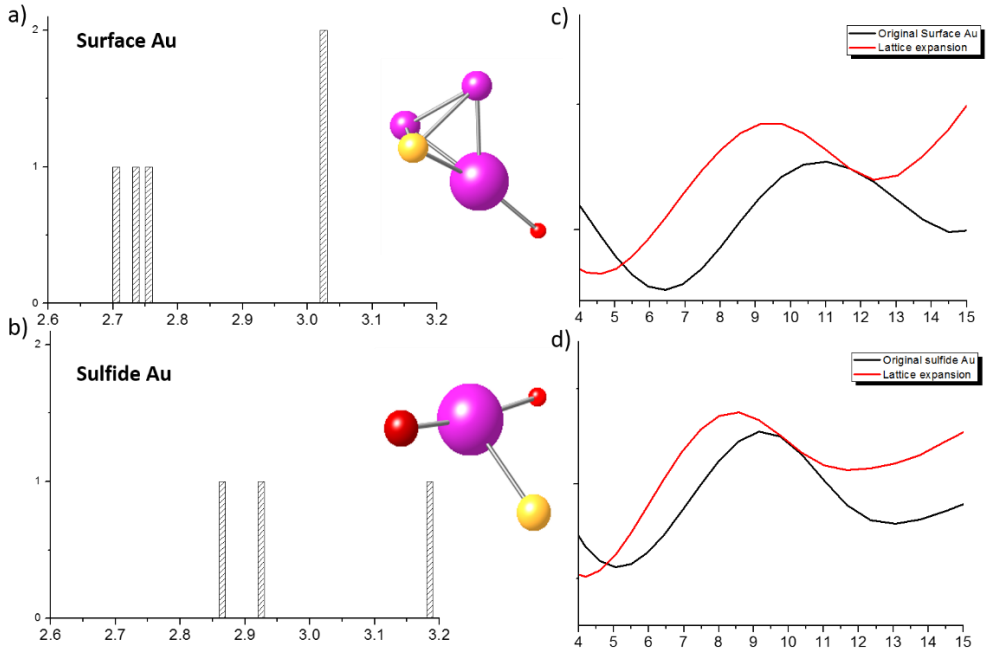


**Figure 5 - 4. Bond distance distribution of surface sites in a) surface Au and b) sulfide Au; The corresponding surface and sulfide sites are exhibited on the right (the selected surface Au atoms are enlarged; yellow: central Au; purple: surface Au; red: surface; enlarged red: sulfide atoms). The simulated bond distance tests of c) surface A and d) surface B are exhibited.**

### 5.3.2 EXAFS analysis

The FT-EXAFS of BCC-$Au_{38}$ and biico-$Au_{38}$, collected at RT, are plotted in Figure

5-5. The most intense peaks that overlap around 2 Å represent Au-S scattering. The peaks caused by Au-Au scatterings are presented around 2.5 Å and 2.7 Å. The less intense peaks in BCC-$Au_{38}$ is consistent to its more molecular-like structure. These features from Au-S and Au-Au scatterings do not show the accurate bonding properties. More detailed structural information of these scattering shells in $Au_{30}$ will be obtained by the refinement of FT-EXAFS.

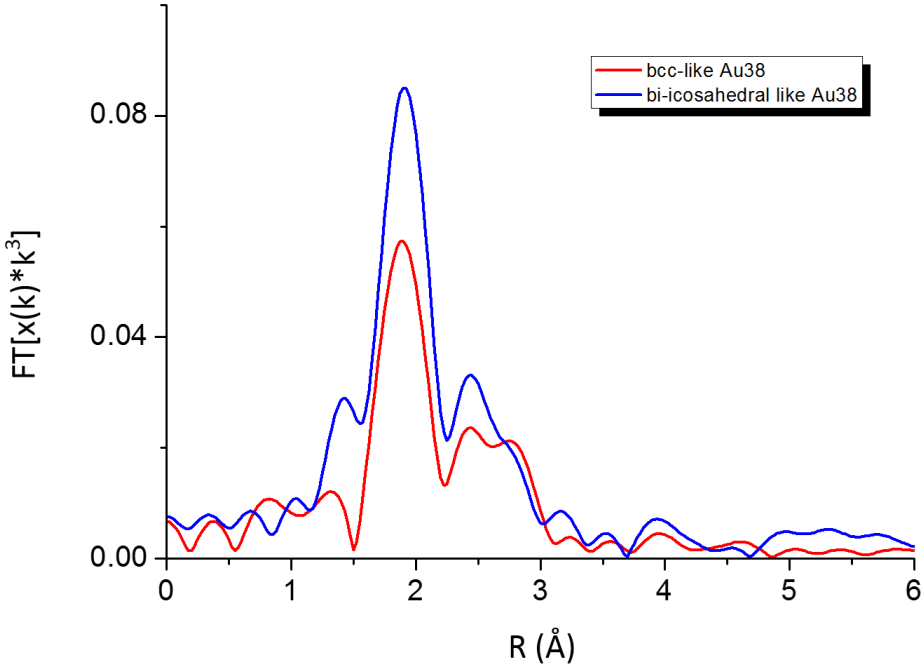


**Figure 5 - 5. Experimental FT-EXAFS of BCC-$Au_{38}$ and biico-$Au_{38}$ (k-range: 3.4 - 12.1 Å).**

Before performing the refinement of FT-EXAFS, the theoretical CN was calculated based on the bond distance distribution. The averaged CN for Au-S, Au-$Au_1$, Au-$Au_2$ scattering shells are 1.2 ((46 Au-S bonds) / 38 Au atoms), 2.5 ((48 Au-Au bonds) * 2 / 38 Au atoms) and 1.1 ((21 Au-Au bonds) * 2 / 38 Au atoms) respectively.

The calculated theoretical CNs of the three shells are then used as the fixed CN values in the EXAFS refinement process. Moreover, it helps us to confirm the three-shell Au $L_3$-edge EXAFS between the two NCs is comparable.

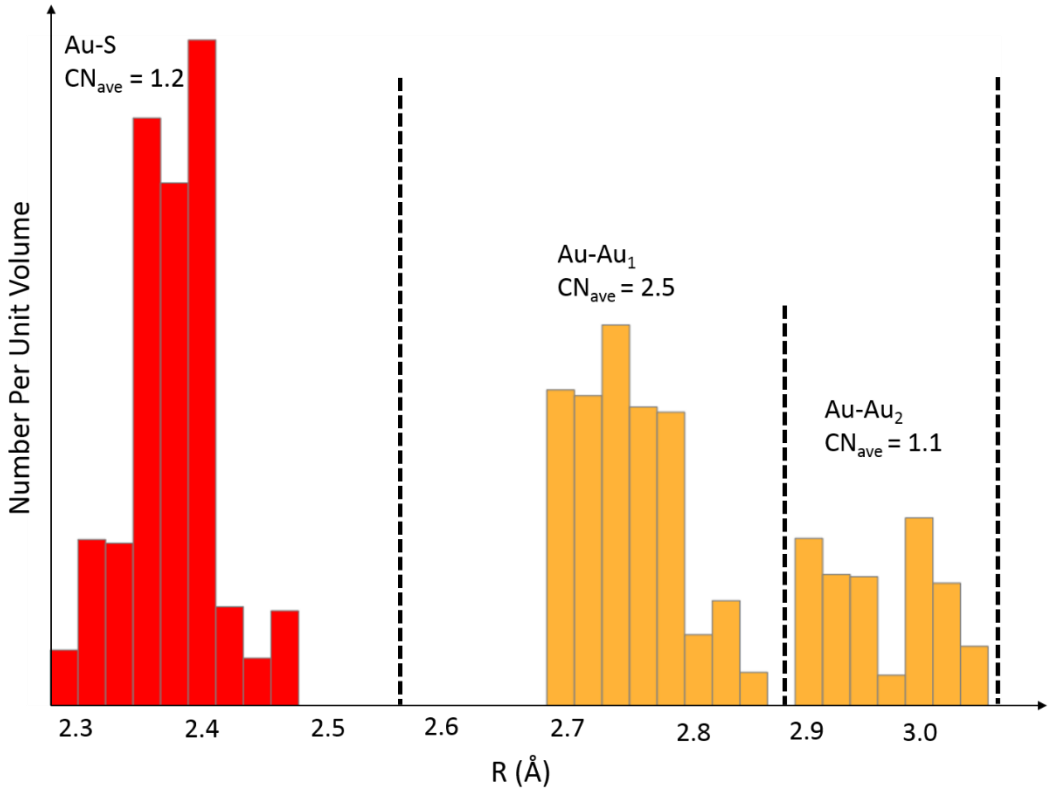


**Figure 5 - 6. Bond distribution for $Au_{38}$ and representative EXAFS scattering shells.**

A three-shell Au $L_3$-edge EXAFS (Au-S, Au-$Au_1$, Au-$Au_2$) fitting was performed on both solid and liquid BCC-$Au_{38}$ at 298 K (RT). Figure 5-7 shows the best fits and their fitting results are recorded in Table 5-1.

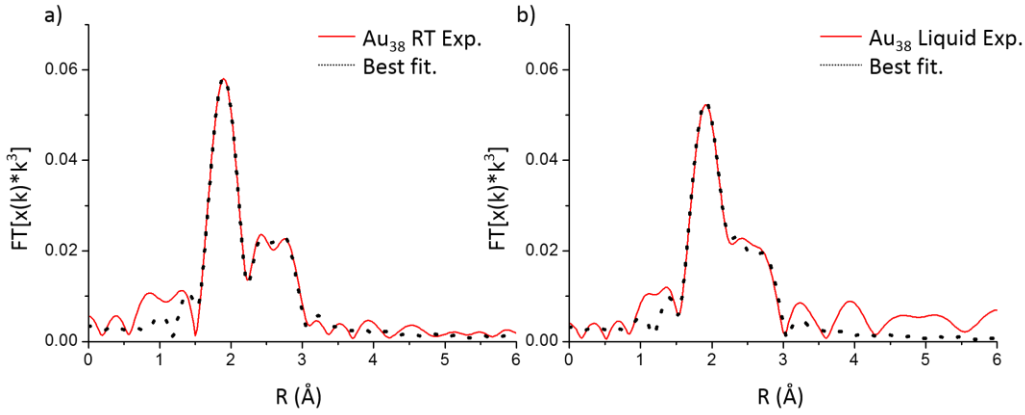


**Figure 5 - 7. Experimental FT-EXAFS (k-range: 3.0-12.3 Å) and best fit for (a) solid and (b) liquid BCC-$Au_{38}$ at RT.**

As shown in the Table 5-1, shorter Au-Au bonds (Au-$Au_1$: ~ 2.7 Å) corresponds to the interactions between central Au and surface Au, whereas the longer Au-Au bonds come from the surface-surface and surface-staple Au interactions. Compared to solid phase, shorter Au-$Au_1$ (decrement = 0.02 Å) and Au-$Au_2$ (decrement = 0.03 Å) bonds are found upon cluster solvation. The more pronounced decrease in Au-$Au_2$ bonding indicates that the out-shell Au-Au bonds are more sensitive to the change of the surface environment.

To gain a better understanding of the findings in BCC-$Au_{38}$, the quantitative structural information of solid and liquid biico-$Au_{38}$, obtained by MacDonald et al, is used as a comparison.[96] In Figure 5-8, it is found that both Au-$Au_1$ and Au-$Au_2$ in BCC-$Au_{38}$ show longer Au-Au bond distances than those in biico-$Au_{38}$.

**Table 5 - 1. EXAFS multi-shell fitting results of BCC-$Au_{38}$ in solid and solution-phase.**

| Phases | Shells | CN | R (Å) | $\sigma^2$ ($Å^2$) | $\Delta E_0$ (eV) |
|---|---|---|---|---|---|
| Solid (RT) | Au-S | 1.2 | 2.312 (4) | 0.0034 (1) | 4 (1) |
| | Au-$Au_1$ | 2.5 | 2.72 (1) | 0.0064 (6) | 4 (1) |
| | Au-$Au_2$ | 1.1 | 2.89 (2) | 0.009 (3) | 4 (1) |
| Solution (RT) | Au-S | 1.2 | 2.330 (9) | 0.0043 (5) | 5 (2) |
| | Au-$Au_1$ | 2.5 | 2.70 (2) | 0.006 (1) | 5 (2) |
| | Au-$Au_2$ | 1.1 | 2.86 (4) | 0.006 (3) | 5 (2) |

**[a] CN values are fixed to the values calculated from total structure (No errors for fixed CN values).**

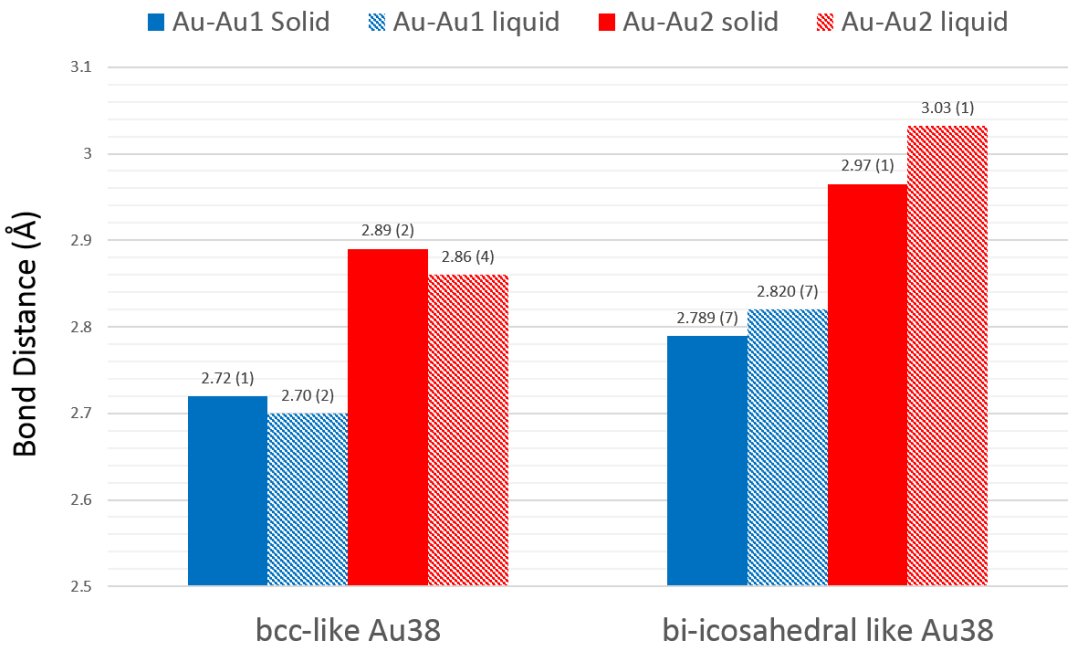


**Figure 5 - 8. Bond distance comparison of Au-$Au_1$, Au-$Au_2$ in BCC-$Au_{38}$ and biico-$Au_{38}$ in both solid and liquid phases.**

Next, the quantitative structural information of solid and liquid biico-$Au_{38}$ is shown on the right in Figure 5-8. In comparison with solid NCs, both Au-$Au_1$ and Au-$Au_2$ in biico-$Au_{38}$ present Au-Au bond expansion in solution-phase. Specifically, increments of 0.03 Å and 0.06 Å are found in Au-$Au_1$ and Au-$Au_2$, respectively. Based on the explanation from previous work by MacDonald et al, the bond expansion in biico-$Au_{38}$ is caused by the interaction between -$CH_2CH_2Ph$ moiety in thiolate ligand and solvent (toluene). To achieve a more stable system between ligand and solvent, Au-Au bonds and Au-S bonds exhibit expansion.[96] In our case, the thiolate ligands (-$C_{10}H_{15}$) in BCC-$Au_{38}$ have weaker $\pi - \pi$ interactions with solvent (toluene). Therefore, the Au-Au shells will not change too much due to the less influence from ligand-solvent interactions. However, a conclusive mechanism has to be provided by further studies.

## 5.4 Conclusions

In summary, the electronic and bonding properties of BCC-like $Au_{38}S_2(SR)_{20}$ nanoclusters were studied by comparing with bi-icosahedral like $Au_{38}S_2(SR)_{20}$ by using XAS. Based on the results from first derivative XANES in association with theoretical calculations, Au-Au bond distance from surface site, which consists of $Au_4$ units, play an important role in influencing the early region of near edge. Furthermore, EXAFS analysis shows significant shorter Au-$Au_1$ and Au-$Au_2$ bond distances in

BCC-like $Au_{38}S_2(SR)_{20}$ compared with those in bi-icosahedral like $Au_{38}(SR)_{24}$. The contraction of Au-Au bonding upon solvation suggests the importance of thiolate ligand type in influencing the bonding properties.

# Chapter 6 – Conclusion

## 6.1 Conclusion

This thesis presents the results on local structure and bonding properties of $Au_{44}(SR)_{28}$, $Au_{30}(SR)_{18}$ and $Au_{38}S_2(SR)_{20}$ studied by XANES and EXAFS.

In the study of FCC-like $Au_{44}(SR)_{28}$, its experimental XAS was compared with two other FCC-like NCs of smaller size: $Au_{28}(SR)_{20}$ and $Au_{36}(SR)_{24}$ NCs. Based on a qualitative comparison of the FT-EXAFS at Au $L_3$-edge, these NCs were found to have similar local structure. The temperature-dependent EXAFS fitting performed on $Au_{44}(SR)_{28}$ indicated the existence of negative thermal expansion (NTE) in the Au-$Au_1$ shell. Furthermore, a size-dependent trend of NTE was found in the three FCC-like Au NCs. The NCs with larger size show a more pronounced NTE in the Au-$Au_1$ shell. This phenomenon was explained by the less perfectly maintained $Au_4$-units within the NCs, which makes the core structure less rigid and thus exhibit more pronounced structural change when the temperature was varied.

The research on HCP-like $Au_{30}(SR)_{18}$ was carried out using XAS by comparing with FCC-like $Au_{36}(SR)_{24}$ and icosahedral-like $Au_{25}(SR)_{18}$. Based on XANES analysis, the early region of XANES was found to be significantly influenced by Au-Au bond distance in surface sites. The temperature-dependent EXAFS indicated that the NTE in Au-$Au_1$ shell of molecular-like $Au_{30}(SR)_{18}$ and $Au_{36}(SR)_{24}$ is strongly

determined by the defects in gold cores. The positive thermal expansion in more metal-like $Au_{25}(SR)_{18}$ is mainly caused by the special metallicity with more rigid and staple character.

In the study of BCC-like $Au_{38}S_2(SR)_{20}$, bi-icosahedral like $Au_{38}(SR)_{24}$ was used as a comparison. By using XAS measurement, the early region of XANES was mainly affected by Au-Au bond distance in surface sites. Based on EXAFS analysis, the significant shorter bond distance in $Au\text{-}Au_1$ and $Au\text{-}Au_2$ of BCC-like $Au_{38}S_2(SR)_{20}$ indicated an obvious different structure. The contraction of Au-Au bond distance upon solvation is probably caused by the thiolate ligand type which may produce different responses from the AuNC structure.

## 6.2 Future Work

The study of $Au_{44}(SR)_{28}$ shows the size-dependent trend of NTE within the three FCC-like Au NCs including $Au_{28}(SR)_{20}$, $Au_{36}(SR)_{24}$ and $Au_{44}(SR)_{28}$. In the future, the temperature-dependent EXAFS of $Au_{52}(SR)_{32}$, another FCC-like Au NC, can be collected to study the size-dependent trend of NTE. Furthermore, the structure of $Au_{52}(SR)_{32}$ (Figure 6-1) and fitting results may help to understand the mechanism of NC growth when its size increases.

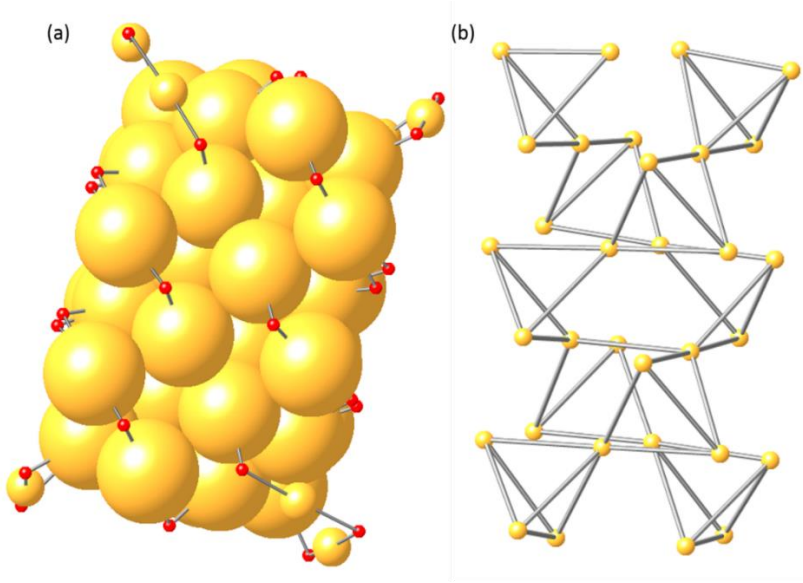


**Figure 6 - 1. (a) Structure model of $Au_{52}(SR)_{32}$. (b) Core structure of $Au_{52}(SR)_{32}$ with first Au-Au scattering shell.**

In the study of HCP-like $Au_{30}(SR)_{18}$, the bonding properties was probed by comparing with FCC-like and icosahedral-like Au NCs. In future work, $Au_{30}(SR)_{18}$ can be compared with other HCP-like thiolate-protected Au NCs to have a better understanding of the trend in HCP-like Au NCs.

The research on BCC-like $Au_{38}S_2(SR)_{20}$ indicates negative expansion of Au-Au bond distance upon solvation. To have a more reliable origin on the results, Au NCs with different thiolate ligand types will be tested, and more evidence will be provided in the future.

# Bibliography


(1) Silva, G. A. Neuroscience Nanotechnology: Progress, Opportunities and Challenges. *Nat. Rev. Neurosci.* **2006**, *7*, 65.

(2) Eustis, S.; El-Sayed, M. a. Why Gold Nanoparticles Are More Precious than Pretty Gold: Noble Metal Surface Plasmon Resonance and Its Enhancement of the Radiative and Nonradiative Properties of Nanocrystals of Different Shapes. *Chem. Soc. Rev.* **2006**, *35*, 209.

(3) Riwotzki, K.; Haase, M. Wet-Chemical Synthesis of Doped Colloidal Nanoparticles: YVO4:Ln (Ln = Eu, Sm, Dy). *J. Phys. Chem. B* **1998**, *102*, 10129.

(4) Jin, R. The Impacts of Nanotechnology on Catalysis by Precious Metal Nanoparticles. *Nanotechnol. Rev.* **2012**, *1*, 31–56.

(5) Temer, S.; Zhong, L.; Travis, C.; Mostafa, A. Shape-Controlled Synthesis of Colloidal Platinum Nanoparticles. *Science.* **1996**, *272*, 1924.

(6) Xiong, Y.; Wiley, B. J.; Xia, Y. Nanocrystals with Unconventional Shapes - A Class of Promising Catalysts. *Angew. Chemie - Int. Ed.* **2007**, *46*, 7157.

(7) Zheng, N.; Stucky, G. D. Communication A General Synthetic Strategy for Oxide-Supported Metal Nanoparticle Catalysts A General Synthetic Strategy for Oxide-Supported Metal Nanoparticle Catalysts. *J. Am. Chem. Soc.* **2006**, *128*, 14278.

(8) Yang, W.; Liu, X.; Yue, X.; Jia, J.; Guo, S. Bamboo-like Carbon nanotube/Fe3C Nanoparticle Hybrids and Their Highly Efficient Catalysis for Oxygen Reduction. *J. Am. Chem. Soc.* **2015**, *137*, 1436.

(9) Sun, X.; Zhao, Y.; Lin, V. S. Y.; Slowing, I. I.; Trewyn, B. G. Luciferase and Luciferin Co-Immobilized Mesoporous Silica Nanoparticle Materials for Intracellular Biocatalysis. *J. Am. Chem. Soc.* **2011**, *133*, 18554.

(10) Liu, Z.; Ling, X. Y.; Su, X.; Lee, J. Y. Carbon-Supported Pt and PtRu Nanoparticles as Catalysts for a Direct Methanol Fuel Cell. *J. Phys. Chem. B* **2004**, *108*, 8234.

(11) Li, L.; Xing, Y. Pt-Ru Nanoparticles Supported on Carbon Nanotubes as Methanol Fuel Cell Catalysts. *J. Phys. Chem. C* **2007**, *111*, 2803.

(12) Mani, P.; Srivastava, R.; Strasser, P. Dealloyed Pt-Cu Core-Shell Nanoparticle Electrocatalysts for Use in PEM Fuel Cell Cathodes. *J. Phys. Chem. C* **2008**,

*112*, 2770.

(13) Chevrier, D. M.; Yang, R.; Chatt, A.; Zhang, P. Bonding Properties of Thiolate-Protected Gold Nanoclusters and Structural Analogs from X-Ray Absorption Spectroscopy. *Nanotechnol. Rev.* **2015**, *4*, 193.

(14) Jain, P. K.; Huang, X.; El-Sayed, I. H.; El-Sayed, M. A. Review of Some Interesting Surface Plasmon Resonance-Enhanced Properties of Noble Metal Nanoparticles and Their Applications to Biosystems. *Plasmonics* **2007**, *2*, 107.

(15) Mie, G. Beiträge Zur Optik Trüber Medien, Speziell Kolloidaler Metallösungen. *Ann. Phys.* **1908**, *330*, 377.

(16) Hagfeldt, A.; Graetzel, M. Light-Induced Redox Reactions in Nanocrystalline Systems. *Chem. Rev.* **1995**, *95*, 49.

(17) Gou, X.; Wang, G.; Park, J.; Liu, H.; Yang, J. Monodisperse Hematite Porous Nanospheres: Synthesis, Characterization, and Applications for Gas Sensors. *Nanotechnology* **2008**, *19*, 125606.

(18) Gudiksen, M. S.; Lauhon, L. J.; Wang, J.; Smith, D. C.; Lieber, C. M. Growth of Nanowire Superlattice Structures for Nanoscale Photonics and Electronics. *Nature* **2002**, *415*, 617.

(19) Dai, H. Carbon Nanotubes: Synthesis, Integration, and Properties. *Acc. Chem. Res.* **2002**, *35*, 1035.

(20) Pérez-Juste, J.; Pastoriza-Santos, I.; Liz-Marzán, L. M.; Mulvaney, P. Gold Nanorods: Synthesis, Characterization and Applications. *Coord. Chem. Rev.* **2005**, *249*, 1870.

(21) Zhang, J.; Yang, H.; Yang, K.; Fang, J.; Zou, S.; Luo, Z.; Wang, H.; Bae, I. T.; Jung, D. Y. Monodisperse Pt3Fe Nanocubes: Synthesis, Characterization, Self-Assembly, and Electrocatalytic Activity. *Adv. Funct. Mater.* **2010**, *20*, 3727.

(22) Gifford, L. K.; Sendroiu, I. E.; Corn, R. M.; Lupt??k, A. Attomole Detection of Mesophilic DNA Polymerase Products by Nanoparticle-Enhanced Surface Plasmon Resonance Imaging on Glassified Gold Surfaces. *J. Am. Chem. Soc.* **2010**, *132*, 9265.

(23) Xie, J.; Liu, G.; Eden, H. S.; Ai, H.; Chen, X. Surface-Engineered Magnetic Nanoparticle Platforms for Cancer Imaging and Therapy. *Acc. Chem. Res.* **2011**, *44*, 883.

(24) Jiang, Z.; Wen, G.; Luo, Y.; Zhang, X.; Liu, Q.; Liang, A. A New Silver Nanorod SPR Probe for Detection of Trace Benzoyl Peroxide. *Sci. Rep.* **2014**,

*4*, 1.

(25) Peng, H. I.; Krauss, T. D.; Miller, B. L. Aging Induced Ag Nanoparticle Rearrangement under Ambient Atmosphere and Consequences for Nanoparticle-Enhanced DNA Biosensing. *Anal. Chem.* **2010**, *82*, 8664.

(26) Su, S.; Sun, H.; Cao, W.; Chao, J.; Peng, H.; Zuo, X.; Yuwen, L.; Fan, C.; Wang, L. Dual-Target Electrochemical Biosensing Based on DNA Structural Switching on Gold Nanoparticle-Decorated MoS2 Nanosheets. *ACS Appl. Mater. Interfaces* **2016**, *8*, 6826.

(27) Petryayeva, E.; Krull, U. J. Quantum Dot and Gold Nanoparticle Immobilization for Biosensing Applications Using Multidentate Imidazole Surface Ligands. *Langmuir* **2012**, *28*, 13943.

(28) Hutchings, G. J.; Brust, M.; Schmidbaur, H. Gold--an Introductory Perspective. *Chem. Soc. Rev.* **2008**, *37*, 1759.

(29) Graham, T. Liquid Diffusion Applied to Analysis. *Philos. Trans. R. Soc. London* **1861**, *151*, 183.

(30) Daniel, M. C. M.; Astruc, D. Gold Nanoparticles: Assembly, Supramolecular Chemistry, Quantum-Size Related Properties and Applications toward Biology, Catalysis and Nanotechnology,. *Chem. Rev.* **2004**, *104*, 293.

(31) Brust, M.; Walker, M.; Bethell, D.; Schiffrin, D. J.; Whyman, R. Synthesis of Thiol-Derivatised Gold Nanoparticles in a Two-Phase Liquid-Liquid System. *Chem. Commun.* **1994**, 801.

(32) Gole, A.; Murphy, C. J. Seed-Mediated Synthesis of Gold Nanorods: Role of the Size and Nature of the Seed. *Chem. Mater.* **2004**, *16*, 3633.

(33) Lu, L.; Suresh, S.; Weertman, J. R.; Zhou, F.; Lavernia, E. J.; He, D. W.; Zhu, Y. T.; Sui, M. L.; Lu, K.; Shen, Y.; Chen, X.; Qian, L.; Chen, M.; Willard, M. a; Laughlin, D. E.; Selvam, R. P.; Saxena, A.; Cheng, H.; Asl, K. M.; Kiely, C. J.; Harmer, M. P.; Chatain, D.; Kaplan, W. D.; Schuh, C. a; Isheim, D.; Kirchheim, R.; Muller, F.; Kreye, H.; Klement, U. Stepwise Evolution of Spherical Seedsinto 20-Fold Twinned Icosahedra. *Science.* **2012**, *337*, 954.

(34) Yang, X.; Yang, M.; Pang, B.; Vara, M.; Xia, Y. Gold Nanomaterials at Work in Biomedicine. *Chem. Rev.* **2015**, *115*, 10410.

(35) Yong, K. T.; Swihart, M. T.; Ding, H.; Prasad, P. N. Preparation of Gold Nanoparticles and Their Applications in Anisotropic Nanoparticle Synthesis and Bioimaging. *Plasmonics* **2009**, *4*, 79.

(36) Cheng, K.; Kothapalli, S. R.; Liu, H.; Koh, A. L.; Jokerst, J. V.; Jiang, H.;

Yang, M.; Li, J.; Levi, J.; Wu, J. C.; Gambhir, S. S.; Cheng, Z. Construction and Validation of Nano Gold Tripods for Molecular Imaging of Living Subjects. *J. Am. Chem. Soc.* **2014**, *136*, 3560.

(37) Shankar, S. S.; Rai, A.; Ahmad, A.; Sastry, M. Controlling the Optical Properties of Lemongrass Extract Synthesized Gold Nanotriangles and Potential Application in Infrared-Absorbing Optical Coatings. *Chem. Mater.* **2005**, *17*, 566.

(38) El-Sayed, I. H.; Huang, X.; El-Sayed, M. A. Surface Plasmon Resonance Scattering and Absorption of Anti-EGFR Antibody Conjugated Gold Nanoparticles in Cancer Diagnostics: Applications in Oral Cancer. *Nano Lett.* **2005**, *5*, 829.

(39) Haruta, M.; Kobayashi, T.; Sano, H.; Yamada, N. Novel Gold Catalysts for the Oxidation of Carbon Monoxide at a Temperature Far below 0.DEG.C. *Chem. Lett.* **1987**, 405.

(40) Hutchings, G. J. Vapor Phase Hydrochlorination of Acetylene: Correlation of Catalytic Activity of Supported Metal Chloride Catalysts. *J. Catal.* **1985**, *96*, 292.

(41) Chevrier, D. M.; Chatt, A.; Zhang, P. Properties and Applications of Protein-Stabilized Fluorescent Gold Nanoclusters : Short Review. *J. Nanophotonics* **2012**, *6*, 64504.

(42) Walter, M.; Akola, J.; Lopez-Acevedo, O.; Jadzinsky, P. D.; Calero, G.; Ackerson, C. J.; Whetten, R. L.; Grönbeck, H.; Häkkinen, H. A Unified View of Ligand-Protected Gold Clusters as Superatom Complexes. *Proc. Natl. Acad. Sci.* **2008**, *105*, 9157.

(43) Pensa, E.; Cortés, E.; Corthey, G.; Carro, P.; Vericat, C.; Fonticelli, M. H.; Benítez, G.; Rubert, A. A.; Salvarezza, R. C. The Chemistry of the Sulfur-Gold Interface: In Search of a Unified Model. *Acc. Chem. Res.* **2012**, *45*, 1183–1192.

(44) Jin, R. Quantum Sized, Thiolate-Protected Gold Nanoclusters. *Nanoscale* **2010**, *2*, 343.

(45) Liu, J.; Krishna, K. S.; Losovyj, Y. B.; Chattopadhyay, S.; Lozova, N.; Miller, J. T.; Spivey, J. J.; Kumar, C. S. S. R. Ligand-Stabilized and Atomically Precise Gold Nanocluster Catalysis: A Case Study for Correlating Fundamental Electronic Properties with Catalysis. *Chemistry* **2013**, *19*, 10201–10208.

(46) Shivhare, A.; Chevrier, D. M.; Purves, R. W.; Scott, R. W. J. Following the

Thermal Activation of Au 25 (SR) 18 Clusters for Catalysis by X‐Ray Absorption Spectroscopy. **2013**, *25*.

(47) Wang, J.; Zhang, G.; Li, Q.; Jiang, H.; Liu, C.; Amatore, C.; Wang, X. In Vivo Self-Bio-Imaging of Tumors through in Situ Biosynthesized Fluorescent Gold Nanoclusters. *Sci. Rep.* **2013**, *3*, 1.

(48) Zhang, P. X-Ray Spectroscopy of Gold–Thiolate Nanoclusters. *J. Phys. Chem. C* **2014**, *118*, 25291–25299.

(49) Cluskey, P. D.; Newport, R. J.; Benfield, R. E.; Gurman, S. J.; Schmid, G. An EXAFS Study of Some Gold and Palladium Cluster Compounds. In *Atoms, Molecules and Clusters*; 1993; Vol. 11, pp. 8–11.

(50) Kurashige, W.; Yamaguchi, M.; Nobusada, K.; Negishi, Y. Ligand-Induced Stability of Gold Nanoclusters: Thiolate versus Selenolate. *J. Phys. Chem. Lett.* **2012**, *3*, 2649–2652.

(51) Simms, G. A.; Padmos, J. D.; Zhang, P. Structural and Electronic Properties of Protein/thiolate-Protected Gold Nanocluster With "staple" motif: A XAS, L-DOS, and XPS Study. *J. Chem. Phys.* **2009**, *131*, 214703.

(52) Xie, J.; Zheng, Y.; Ying, J. Y. Protein-Directed Synthesis of Highly Fluorescent Gold Nanoclusters. *J. Am. Chem. Soc.* **2009**, *131*, 888.

(53) Schmid, G. Large Clusters and Colloids. Metals in the Embryonic State. *Chem. Rev.* **1992**, *92*, 1709.

(54) Knoppe, S.; Boudon, J.; Dolamic, I.; Dass, A.; Bürgi, T. Size Exclusion Chromatography for Semipreparative Scale Separation of Au38(SR)24 and Au40(SR)24 and Larger Clusters. *Anal. Chem.* **2011**, *83*, 5056–5061.

(55) Qian, H.; Zhu, Y.; Jin, R. Isolation of Ubiquitous Au40(SR)24 Clusters from the 8 kDa Gold Clusters. *J. Am. Chem. Soc.* **2010**, *132*, 4583.

(56) Chen, Y.; Zeng, C.; Kauffman, D. R.; Jin, R. Tuning the Magic Size of Atomically Precise Gold Nanoclusters via Isomeric Methylbenzenethiols. *Nano Lett.* **2015**, *15*, 3603.

(57) Yu, Y.; Chen, X.; Yao, Q.; Yu, Y.; Yan, N.; Xie, J. Scalable and Precise Synthesis of Thiolated Au10-12, Au15, Au18, and Au25 Nanoclusters via pH Controlled CO Reduction. *Chem. Mater.* **2013**, *25*, 946.

(58) Negishi, Y.; Nobusada, K.; Tsukuda, T. Glutathione-Protected Gold Clusters Revisited: Bridging the Gap between gold(I)-Thiolate Complexes and Thiolate-Protected Gold Nanocrystals. *J. Am. Chem. Soc.* **2005**, *127*, 5261.

(59) Dass, A.; Theivendran, S.; Nimmala, P. R.; Kumara, C.; Jupally, V. R.;

Fortunelli, A.; Sementa, L.; Barcaro, G.; Zuo, X. B.; Noll, B. C. Au133(SPh-tBu)52 Nanomolecules: X-Ray Crystallography, Optical, Electrochemical, and Theoretical Analysis. *J. Am. Chem. Soc.* **2015**, *137*, 4610.

(60) Zeng, C.; Chen, Y.; Kirschbaum, K.; Appavoo, K.; Sfeir, M. Y.; Jin, R. Structural Patterns at All Scales in a Nonmetallic Chiral Au133(SR)52 Nanoparticle. *Sci. Adv.* **2015**, *1*, 1500045.

(61) Chen, Y.; Zeng, C.; Liu, C.; Kirschbaum, K.; Gayathri, C.; Gil, R. R.; Rosi, N. L.; Jin, R. Crystal Structure of Barrel-Shaped Chiral Au130(p-MBT)50 Nanocluster. *J. Am. Chem. Soc.* **2015**, *130*, 10076.

(62) Tang, Z.; Robinson, D. A.; Bokossa, N.; Xu, B.; Wang, S.; Wang, G. Mixed Dithiolate Durene-DT and Monothiolate Phenylethanethiolate Protected Au130 Nanoparticles with Discrete Core and Core-Ligand Energy States. *J. Am. Chem. Soc.* **2011**, *133*, 16037.

(63) Zeng, C.; Chen, Y.; Li, G.; Jin, R. Synthesis of a Au44(SR)28 Nanocluster: Structure Prediction and Evolution from Au28(SR)20, Au36(SR)24 to Au44(SR)28. *Chem. Commun.* **2014**, *50*, 55.

(64) Zeng, C.; Chen, Y.; Liu, C.; Nobusada, K.; Rosi, N. L.; Jin, R. Gold Tetrahedra Coil up: Kekule-like and Double Helical Superstructures. *Sci. Adv.* **2015**, *1*, 1500425.

(65) Zhu, Y.; Qian, H.; Zhu, M.; Jin, R. Thiolate-Protected Aun Nanoclusters as Catalysts for Selective Oxidation and Hydrogenation Processes. *Adv. Mater.* **2010**, *22*, 1915.

(66) Zeng, C.; Chen, Y.; Iida, K.; Nobusada, K.; Kirschbaum, K.; Lambright, K. J.; Jin, R. Gold Quantum Boxes: On the Periodicities and the Quantum Confinement in the Au28, Au36, Au44, and Au52 Magic Series. *J. Am. Chem. Soc.* **2016**, *138*, 3950.

(67) Das, A.; Li, T.; Nobusada, K.; Zeng, C.; Rosi, N. L.; Jin, R. Nonsuperatomic [Au23(SC6H11)16]- Nanocluster Featuring Bipyramidal Au15 Kernel and Trimeric Au3(SR)4 Motif. *J. Am. Chem. Soc.* **2013**, *135*, 18264.

(68) Das, A.; Liu, C.; Byun, H. Y.; Nobusada, K.; Zhao, S.; Rosi, N.; Jin, R. Structure Determination of [Au18(SR)14]. *Angew. Chemie - Int. Ed.* **2015**, *54*, 3140.

(69) Crasto, D.; Malola, S.; Brosofsky, G.; Dass, A.; Hakkinen, H. Single Crystal XRD Structure and Theoretical Analysis of the Chiral Au30S(S-T-Bu)18 Cluster. *J. Am. Chem. Soc.* **2014**, *136*, 5000.

(70) Das, A.; Li, T.; Li, G.; Nobusada, K.; Zeng, C.; Rosi, N. L.; Jin, R. Crystal

Structure and Electronic Properties of a Thiolate-Protected Au24 Nanocluster. *Nanoscale* **2014**, *6*, 6458.

(71) Jadzinsky, P. D.; Calero, G.; Ackerson, C. J.; Bushnell, D. A.; Kornberg, R. D. Structure of a Thiol Monolayer-Protected Gold Nanoparticle at 1.1 A Resolution. *Science.* **2007**, *318*, 430.

(72) Qian, H.; Eckenhoff, W. T.; Zhu, Y.; Pintauer, T.; Jin, R. Total Structure Determination of Thiolate-Protected Au38 Nanoparticles. *J. Am. Chem. Soc.* **2010**, *132*, 8280.

(73) Zeng, C.; Li, T.; Das, A.; Rosi, N. L.; Jin, R. Chiral Structure of Thiolate-Protected 28-Gold-Atom Nanocluster Determined by X-Ray Crystallography. *J. Am. Chem. Soc.* **2013**, *135*, 10011.

(74) Zhu, M.; Aikens, C. M.; Hollander, F. J.; Schatz, G. C. Correlating the Crystal Structure of A Thiol-Protected Au25 Cluster and Optical Properties. *J. Am. Chem. Soc.* **2008**, *130*, 5883.

(75) Zeng, C.; Liu, C.; Chen, Y.; Rosi, N. L.; Jin, R. Gold-Thiolate Ring as a Protecting Motif in the Au20(SR)16 Nanocluster and Implications. *J. Am. Chem. Soc.* **2014**, *136*, 11922.

(76) Zeng, C.; Qian, H.; Li, T.; Li, G.; Rosi, N. L.; Yoon, B.; Barnett, R. N.; Whetten, R. L.; Landman, U.; Jin, R. Total Structure and Electronic Properties of the Gold Nanocrystal Au36(SR)24. *Angew. Chemie - Int. Ed.* **2012**, *51*, 13114.

(77) Huang, T.; Murray, R. W. Visible Luminescence of Water-Soluble Monolayer-Protected Gold Clusters. *J. Phys. Chem. B* **2001**, *105*, 12498.

(78) Alvarez, M. M.; Khoury, J. T.; Schaaff, T. G.; Shafigullin, M.; Vezmar, I.; Whetten, R. L. Critical Sizes in the Growth of Au Clusters. *Chem. Phys. Lett.* **1997**, *266*, 91.

(79) Hostetler, M. J.; Green, S. J.; Stokes, J. J.; Murray, R. W. Monolayers in Three Dimensions: Synthesis and Electrochemistry of W-Functionalized Alkanethiolate-Stabilized Gold Cluster Compounds. *J. Am. Chem. Soc.* **1996**, *118*, 4212.

(80) Qu, X.; Li, Y.; Li, L.; Wang, Y.; Liang, J.; Liang, J. Fluorescent Gold Nanoclusters : Synthesis and Recent Biological Application. *J. Nanomater.* **2015**, *2015*, 784097.

(81) Chevrier, D. M.; Chatt, A.; Zhang, P.; Zeng, C.; Jin, R. Unique Bonding Properties of the Au36(SR)24 Nanocluster with FCC-Like Core. *J. Phys. Chem. Lett.* **2013**, *4*, 3186.

(82) Chevrier, D. M.; Zeng, C.; Jin, R.; Chatt, A.; Zhang, P. Role of Au4 Units on the Electronic and Bonding Properties of Au28(SR)20 Nanoclusters from X-Ray Spectroscopy. *J. Phys. Chem. C* **2015**, *119*, 1217.

(83) Yang, R.; Chevrier, D. M.; Zeng, C.; Jin, R.; Zhang, P. Bonding Properties of FCC-like Au44(SR)28 Clusters from X-Ray Absorption Spectroscopy. *Can.J.Chem.* **2017**, *95*, 1220.

(84) Liu, C.; Li, T.; Li, G.; Nobusada, K.; Zeng, C.; Pang, G.; Rosi, N. L.; Jin, R. Observation of Body-Centered Cubic Gold Nanocluster. *Angew. Chemie - Int. Ed.* **2015**, *54*, 9826.

(85) Higaki, T.; Liu, C.; Zeng, C.; Jin, R.; Chen, Y.; Rosi, N. L.; Jin, R. Controlling the Atomic Structure of Au30 Nanoclusters by a Ligand-Based Strategy. *Angew. Chemie - Int. Ed.* **2016**, *55*, 6694.

(86) Ankudinov, A. L.; Ravel, B.; Rehr, J. J.; Conradson, S. D. Real-Space Multiple-Scattering Calculation and Interpretation of X-Ray-Absorption near-Edge Structure. *Phys. Rev. B* **1998**, *58*, 7565.

(87) Attwood, D. Soft X-Rays and Extreme Ultraviolet Radiation. *Soft X-Rays Extrem. Ultrav. Radiat. Princ. Appl.* **1999**, 504.

(88) Rehr, J. J.; Albers, R. C. Theoretical Approaches to X-Ray Absorption Fine Structure. *Rev. Mod. Phys.* **2000**, *72*, 621.

(89) Rehr, J. J.; Albers, R. C. Scattering-Matrix Formulation of Curved-Wave Multiple-Scattering Theory: Application to X-Ray-Absorption Fine Structure. *Phys. Rev. B* **1990**, *41*, 8139.

(90) Padmos, J. D.; Zhang, P. Surface Structure of Organosulfur Stabilized Silver Nanoparticles Studied with X-Ray Absorption Spectroscopy. *J. Phys. Chem. C* **2012**, *116*, 23094.

(91) Koningsberger, D. C.; Mojet, B. L.; Dorssen, G. E. Van; Ramaker, D. E. XAFS Spectroscopy; Fundamental Principles and Data Analysis. *Top. Catal.* **2000**, *10*, 143.

(92) Lytle, F. W. The EXAFS Family Tree: A Personal History of the Development of Extended X-Ray Absorption Fine Structure. *J. Synchrotron Radiat.* **1999**, *6*, 123.

(93) E.A.Stern; D.E.Sayers. Extended X-Ray-Absorption Fine-Structure technique.3.Determination of Physical Parameters. *Phys. Rev. B* **1975**, *11*, 4836.

(94) Ressler, T. WinXAS: A Program for X-Ray Absorption Spectroscopy Data

Analysis under MS-Windows. *J. Synchrotron Radiat.* **1998**, *5*, 118.

(95) Macdonald, M. A.; Chevrier, D. M.; Zhang, P.; Qian, H.; Jin, R. The Structure and Bonding of Au25(SR)18 Nanoclusters from EXAFS: The Interplay of Metallic and Molecular Behavior. *J. Phys. Chem. C* **2011**, *115*, 15282.

(96) Macdonald, M. A.; Zhang, P.; Chen, N.; Qian, H.; Jin, R. Solution-Phase Structure and Bonding of Au38(SR)24 Nanoclusters from X-Ray Absorption Spectroscopy. *J. Phys. Chem. C* **2011**, *115*, 65.

(97) Rehr, J. J.; de Leon, J. M.; Zabinsky, S. I.; Albers, R. C. Theoretical X-Ray Absorption Fine-Structure Standards. *J. Am. Chem. Soc.* **1991**, *113*, 5135.

(98) Tian, Z.; Cheng, L. Electronic and Geometric Structures of Au30 Clusters: A Network of 2e-Superatom Au Cores Protected by Tridentate Protecting Motifs with u3-S. *Nanoscale* **2015**, *8*, 826.

(99) Yang, H.; Wang, Y.; Edwards, A. J.; Yan, J.; Zheng, N. High-Yield Synthesis and Crystal Structure of a Green Au30 Cluster Co-Capped by Thiolate and Sulfide. *Chem. Commun.* **2014**, *50*, 14325.

(100) Zhang, P. X-Ray Spectroscopy of Gold–Thiolate Nanoclusters. *J. Phys. Chem. C* **2014**, *118*, 25291.